Effects of aerodynamic coupling and non-linear behaviour on galloping of ice-accreted conductors

Short title: **Galloping of ice-accreted conductors**

Hisato Matsumiya [a, c,*], Tomomi Yagi [b], John H.G. Macdonald [c]

[a] Civil Engineering Research Laboratory, Central Research Institute of Electric Power Industry, Abiko 1646, Abiko-shi, Chiba 270-1194, Japan

[b] Department of Civil and Earth Resources Engineering, Kyoto University, Kyotodaigaku-katsura, Nishikyo-ku, Kyoto 615-8540, Japan

[c] Department of Civil Engineering, University of Bristol, Queen's Building, University Walk, Bristol BS8 1TR, U.K.

*Corresponding author. Tel. / Fax.: +81 4-7182-1181 / +81 4-7184-7142. E-mail ID: hisato-m@criepi.denken.or.jp

Abstract

Wind action on ice-covered transmission lines causes galloping, which is a problem because it can introduce interphase short circuits and cause fatigue of the cross-arms of the power line's towers and insulators. The galloping phenomenon is characterised by a combination of large-amplitude, low-frequency vertical, horizontal, and torsional oscillations. To better understand the dynamic responses of vertical, horizontal and torsional 3-degree-of-freedom (DoF) galloping on four-bundled conductors, time–history analyses were conducted for 2D systems of varying DoFs and frequency ratios. The fundamental characteristics of the conductor's non-linear 1-DoF vertical response were analysed via time–history analysis, indicating that large oscillations were caused by inclusion of an angular range of relative angle of attack with a high negative lift-coefficient slope. By considering the energy balance of the vertical motion over one oscillation period, we estimated the stable and unstable limit-cycle amplitudes. Then, by comparing the results of the 1-, 2-, and 3-DoF systems, we clarified the effect of aerodynamic coupling on 3-DoF galloping. The oscillation types in the 3-DoF systems were categorised as vertical–horizontal 2-DoF coupling oscillations, vertical–torsional 2-DoF coupling oscillations, and vertical 1-DoF oscillations according to the stationary torsional angle. Finally, we indicated the coupling effects on vertical oscillation by considering the energy balance of the vertical motion with the defined amplitudes and phase differences of the horizontal and torsional motions. The vertical amplitude of the vertical–horizontal 2-DoF coupling oscillation can become very large if the horizontal amplitude increases and the phase difference between horizontal and vertical displacements approaches 180°. Meanwhile, the range of the stationary torsional angle in which the vertical–torsional 2-DoF coupling oscillation occurs becomes wide as the phase difference between the torsional and vertical displacements approaches 90°. However, without horizontal motion, the vertical amplitude has a limited value, even if the torsional amplitude becomes large.

Keywords: Aerodynamic coupling, energy balance, four-bundled conductor, galloping amplitude, ice-accretion, overhead transmission lines.

1. Introduction

Galloping is low-frequency, high-amplitude oscillation that occurs in a power or transmission line when a steady wind of moderate velocity flows over cables covered by a layer of ice. The International Council on Large Electric Systems recognises this phenomenon as an aerodynamic instability that can cause interphase short circuits, conductor strand burn, and fatigue failure of the cross-arms of the power line's towers and insulators (CIGRE, 2007). To prevent galloping-related failures and hazards, the location in the power line where the phenomenon is likely to occur, the mode by which it will reach the line, and the amplitude of its motion must be predicted. A solution to the galloping problem should focus not only on the occurrence conditions but also on the oscillation amplitude under various structural conditions. Furthermore, the ice-accretion pattern and wind conditions vary continually with respect to atmospheric parameters. Therefore, several researchers have conducted numerical analyses of full-scale overhead transmission lines (Yu et al., 1993; Desai et al., 1996; Wang and Lillien, 1998; Shimizu et al., 1998; Liu et al., 2009), along with field observations (Morishita et al., 1984; Yukino et al., 1995; Matsumiya et al., 2012; Matsumiya et al., 2019). Different cases should be analysed to understand the roles of the varying parameters related to this phenomenon, including structural characteristics, accretion shape, angles of attack, and wind speed. Accordingly, a theoretical understanding of the conditions that facilitate galloping is necessary for conducting systematic and efficient time–history analyses of the dynamic response of power lines to aerodynamic loading.

In time–history analyses, aerodynamic forces acting on power lines are generally represented as quasi-steady forces using steady-state aerodynamic coefficients. Kimura et al. (1999) highlighted that, during the large-amplitude motion of a four-bundled conductor, the aerodynamic forces exerted on the bundle may differ from the theoretical quasi-steady aerodynamic forces. Therefore, Matsumiya et al. (2018) validated the quasi-steady aerodynamic force formulations applied to a four-bundled conductor by employing the results of large-amplitude-vibration tests. They performed tests in a wind tunnel using a technique in which a rigid-body section model of a four-bundled conductor was supported by multiple elastic cords; the resulting action of the wind (galloping) was studied. They concluded that the quasi-steady aerodynamic forces of a multi-bundled conductor should be formulated independently for each sub-conductor, even when the independent motion of each sub-conductor is not considered.

Den Hartog (1956) identified the conditions under which 1-DoF vertical galloping of an ice-accreted conductor occurs according to the quasi-steady aerodynamic theory. Hence, the galloping criterion is commonly known as the “Den Hartog” criterion. Nakamura (1980) split the instability term of vertical and torsional 2-DoF systems into a 1-DoF and classical-flutter types. The 1-DoF type represents the Den Hartog instability or torsional flutter, whereas the classical-flutter type represents the aerodynamic coupling effect between the motions of each DoF. Nakamura (1980) derived equations to express the contribution of each instability type to the damping term. In contrast, Jones (1992) and Nikitas and Macdonald (2014) discussed the coupling effects of vertical and horizontal oscillations in a galloping conductor with ice-accretion. Furthermore, He and Macdonald (2016) considered a vertical, horizontal, and torsional 3-DoF system and derived an analytical solution for its galloping stability. While this analytical solution was derived assuming that the natural frequencies in the three directions are equal, Lou et al. (2020) derived an analytical galloping stability criterion for 3-DoF coupled motion using the eigenvalue perturbation method.

In contrast with research on the onset conditions (i.e., the damping characteristics), studies on the oscillation amplitude characteristics should focus on solving the galloping problem. In other words, in addition to linear oscillations, research must also focus on non-linear ones. Unfortunately, few studies have focused on the oscillation mechanism and coupling effect between multi-DoF non-linear galloping. Parkinson and Smith (1964) described stable and unstable limit-cycle oscillation amplitudes for a square prism in a vertical 1-DoF system. These are the typical characteristics of a non-linear oscillator that are caused by non-linear aerodynamic forces, which were formulated using the quasi-steady theory with the polynomial expression of aerodynamic coefficients. Novak (1969, 1972) evaluated the effect of mode shapes on the 1-DoF galloping amplitude of long prismatic structures with elastic continuous bodies rather than rigid ones. Blevins and Iwan (1974) and Desai et al. (1990) developed a method to analyse the steady-state amplitude of vertical and torsional 2-DoF coupled galloping. To clarify the conditions facilitating the galloping phenomenon, which is a vertical, horizontal, and torsional 3-DoF oscillation, the aerodynamic coupling effect among the DoF motions should be discussed considering non-linear oscillation characteristics.

In this study, to clarify the essential non-linear response characteristics of a four-bundled conductor to galloping, we conducted a series of time–history analyses on 1-, 2-, and 3-DoF systems by formulating quasi-steady aerodynamic forces on each sub-conductor. To focus on the fundamental effects of aerodynamic coupling and non-linearity on the oscillation amplitude, we used a 2D model instead of a 3D full-span model because the latter considers complex characteristics (i.e., distribution of the angle of ice-accretion and displacements) along the length of the conductor (Yu et al., 1993; Wang and Lillien, 1998). In addition to time–history analyses, the work performed by the aerodynamic force and the energy balance of the vertical motion over one oscillation period were analysed to describe the oscillation mechanism considering aerodynamic non-linearity. From these analyses, we provide a substantial description of the aerodynamic coupling effect between the motions of each DoF and the characteristics of non-linear oscillation caused by non-linear aerodynamic forces.

2. Time–history analysis conditions of a 2D system

2.1 Cross-section and steady aerodynamic coefficients

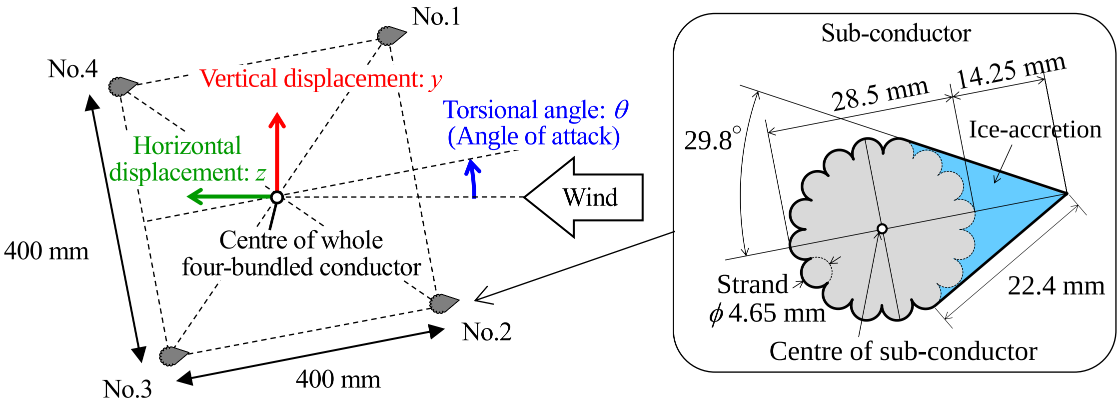

Fig. 1 Cross-sections of ice-accreted four-bundled conductor.

Time–history analyses were conducted for the ice-accreted four-bundled conductor shown in Fig. 1. The dimensions are identical to those of aluminium conductors steel-reinforced (ACSR) conductors having a nominal cross-sectional area of 410 mm^2. For the cases of wet snow accretion and in-cloud ice-accretion, which are the main factors inducing galloping in Japan, accretion develops to the windward side with a sharp edge (Matsumiya et al., 2012; Matsumiya et al., 2019). As a simple imitation of the typical accretion shape, a triangular tip shape was selected for ice-accretion on the sub-conductors in this study.

The steady aerodynamic coefficients of this section were measured via surface pressure-measurement tests (Matsumiya et al., 2011). The aerodynamic coefficients of each sub-conductor and the whole four-bundled conductor are shown in Fig. 2. The equations of the coefficients used in this study are as follows:

$$F_{Di} = \frac{1}{2}\rho U^2 D C_{Di}, F_{Li} = \frac{1}{2}\rho U^2 D C_{Li}, F_{Mi} = \frac{1}{2}\rho U^2 D^2 C_{Mi}, \quad (1)$$

$$F_{Df} = \frac{1}{2}\rho U^2 4D C_{Df}, F_{Lf} = \frac{1}{2}\rho U^2 4D C_{Lf}, F_{Mf} = \frac{1}{2}\rho U^2 4DB C_{Mf}. \quad (2)$$

Here, C_{Di}, C_{Li}, C_{Mi} $(i = 1\text{–}4)$ and C_{Df}, C_{Lf}, C_{Mf} are the aerodynamic coefficients of the respective aerodynamic forces acting on each sub-conductor and four-bundled conductor; $F_{Di}, F_{Li},$ and F_{Mi} are the mean values of the drag, lift, and aerodynamic pitching moment around the centre of sub-conductors No. i $(i = 1\text{–}4)$ per unit length, as shown in Fig. 1, respectively; $F_{Df}, F_{Lf},$ and F_{Mf} are the mean values of drag, lift, and aerodynamic pitching moment around the centre of the whole four-bundled conductor per unit length,

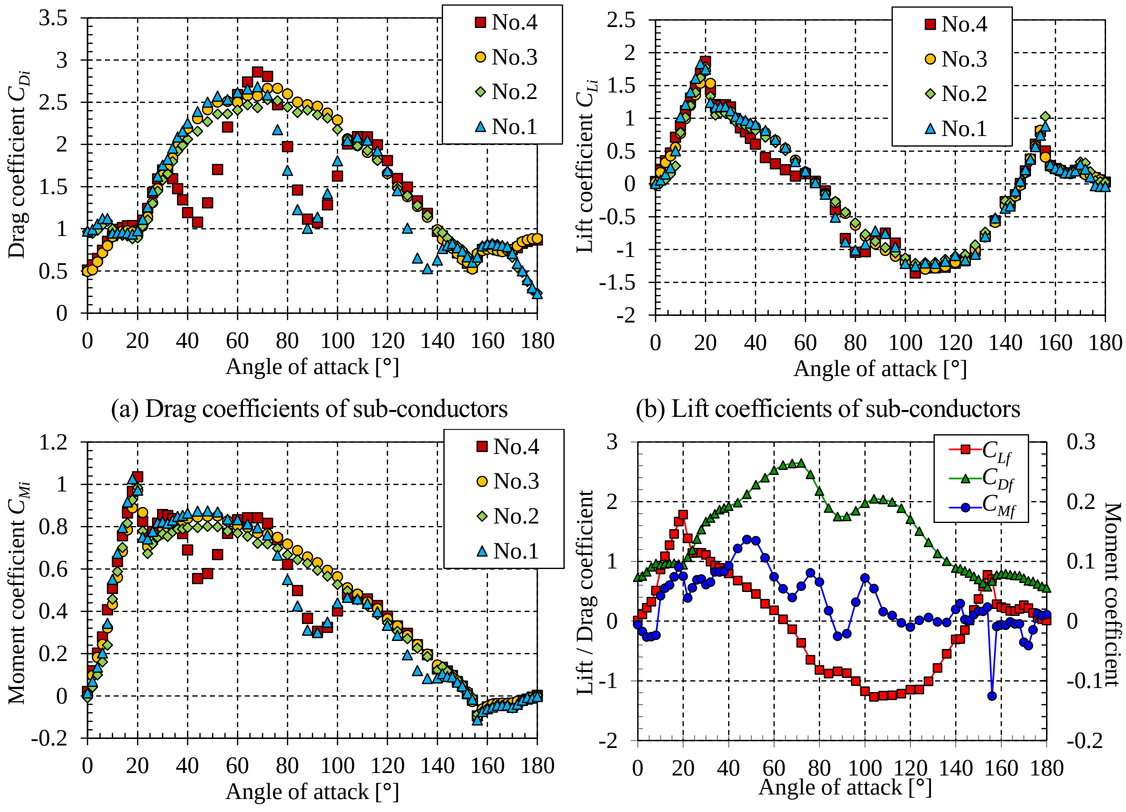

(a) Drag coefficients of sub-conductors (b) Lift coefficients of sub-conductors

(c) Moment coefficients of sub-conductors (d) Aerodynamic coefficients of four-bundled conductor

Fig. 2 Aerodynamic coefficients of ice-accreted four-bundled conductor (Matsumiya et al., 2011)

respectively; ρ is the air density; U is the wind speed; D is the conductor diameter; and B is the spacing between the centres of the sub-conductors.

Figures 2 (b) and (d) show two peaks of the lift coefficient, C_{Li}, at certain angles of attack: one around 20° and the other around 150°. The angles corresponding to the peak lift coefficients are the stalling angles. In the flow field around the sub-conductor, the time-averaged separation shear layer from the upper leading edge of the section reattaches to the conductor surface. Subsequently, a large lift force acts on the conductor when the angle of attack is less than the stalling angle. However, the time-averaged separation shear layer is not reattached to the surface, and the lift force suddenly decreases when the angle of attack is slightly larger than the stalling angle (Matsumiya et al., 2011). A few sub-conductors have lower aerodynamic coefficients than the rest. This is especially true for the drag coefficient. The coefficients exhibit significant reductions at attack

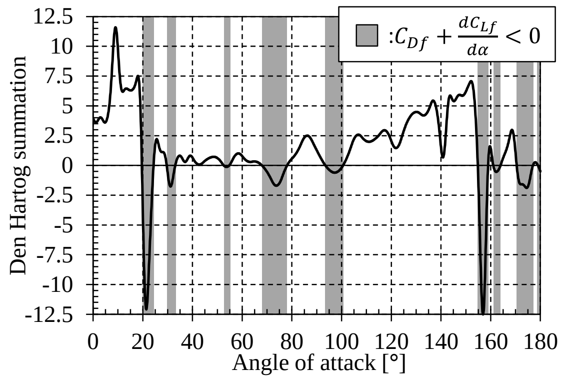

Fig. 3 Den Hartog summation of ice-accreted four-bundled conductor

angles of 0, 45, 90, 135, and 180°. At these angles, the sub-conductor with reduced coefficients lies in the wake of another. Hence, the reduced aerodynamic coefficients of the sub-conductors may be attributed to these wake effects.

Based on linearised quasi-steady aerodynamic theory, vertical 1-DoF galloping occurs when

$$C_{Df} + \frac{\mathrm{d}C_{Lf}}{\mathrm{d}\alpha} < -\frac{m\zeta_{y0}\omega_{y0}}{\rho DU}. \tag{3}$$

Here, m is the mass of the iced-bundled conductor per unit length; ζ_{y0} is the vertical damping ratio; and ω_{y0} is the vertical circular frequency. The left-hand side of the equation corresponds to the Den Hartog summation (1956), and the right-hand side of the equation is negative and proportional to the structural damping. For galloping to occur, a necessary condition is that the summation is negative: this condition is called the Den Hartog criterion. The Den Hartog summation of the four-bundled conductor is shown in Fig. 3. The Den Hartog criterion is mainly fulfilled for angle ranges that are slightly larger than the stalling angles or are under the influence of flow interference between sub-conductors.

2.2 Analysis model and conditions

Time–history analysis was conducted on simple mass–spring–damper 2D systems with varying DoFs. The systems included the vertical 1-DoF, vertical–horizontal 2-DoF, vertical–torsional 2-DoF, and vertical–horizontal–torsional 3-DoF. The equations of 3-DoF motion are expressed as follows:

$$
\begin{aligned}
m\ddot{y} + 2m\zeta_{y0}\omega_{y0}\dot{y} + m\omega_{y0}^2 y &= F_y, \\
m\ddot{z} + 2m\zeta_{z0}\omega_{z0}\dot{z} + m\omega_{z0}^2 z &= F_z, \\
I\ddot{\theta} + 2I\zeta_{\theta 0}\omega_{\theta 0}\dot{\theta} + I\omega_{\theta 0}^2 \theta &= F_\theta.
\end{aligned} \tag{4}
$$

Here, y, z, and θ are the vertical, horizontal, and torsional displacements, respectively (Fig. 1): I is the mass moment of inertia of the ice-bundled conductor per unit length; $\zeta_{q0}(q = y, z, \theta)$ is the damping ratio for each direction; and $\omega_{q0}(q = y, z, \theta)$ is the circular natural frequency for each direction, which is 2π times the natural frequency f_{q0}. The vertical 1-DoF system uses the first expression in Eq. (4). The vertical–horizontal 2-DoF system uses the first and second expressions. The vertical–torsional 2-DoF system uses the first and third expressions. Finally, the vertical–horizontal–torsional 3-DoF system uses all three expressions.

In this study, the horizontal and torsional frequency ratios, f_{z0}/f_{y0} and $f_{\theta 0}/f_{y0}$, were varied, whereas the vertical natural frequency, f_{y0}, remained a constant value that corresponds to the frequency of the first asymmetric mode in an actual transmission line having a span length of 300 m. The parameter values used in this study are presented in Table 1. The mass and mass moment of inertia in the analysis were identical to those of the actual conductors having wet snow accretion using a specific gravity of snow accretion of 0.6. Time–history analysis was performed at a constant wind speed of 10.0 m/s by varying the setup torsional angle, θ_0, in each system. The setup torsional angle corresponds to the angle without wind: the stationary torsional angle with wind, θ_s, is different from θ_0 in the vertical–torsional 2-DoF system and the vertical–horizontal-torsional 3-DoF system. The wind direction is identical to the horizontal axis without a vertical component, as shown in Fig. 1. Because the value of the right-hand side of Eq. (3) is approximately -0.25 in this condition, vertical 1-DoF galloping occurs for almost all of the angle range for which the Den Hartog criterion is fulfilled (Fig. 3).

Table 1 Analysis conditions

Mass of iced-bundled conductor per unit length	m	7.094 kg/m	Wind speed	U	10.0 m/s
Mass moment of inertia of iced-bundled conductor per unit length	I	0.567 kg·m^2/m	Setup torsional angle	θ_0	0 – 180° (in 1° intervals)

Spacing of sub-conductor	B	0.400 m	Vertical damping ratio	ζ_{y0}	0.5 %
Diameter of sub-conductor	D	0.0285 m	Horizontal damping ratio	ζ_{z0}	0.5 %
Vertical natural frequency	f_{y0}	0.393 Hz	Torsional damping ratio	$\zeta_{\theta 0}$	0.5 %
			Air density	ρ	1.225 kg/m^3

F_y, F_z, and F_θ are the aerodynamic forces exerted on the four-bundled conductor in the vertical, horizontal, and torsional directions, respectively. The forces are derived by combining the quasi-steady aerodynamic forces of each sub-conductor, L_{si}, D_{si} and M_{si}, as follows (Matsumiya et al., 2018):

$$\begin{aligned} F_y = \sum_{i=1}^{4} L_{si}, F_z = \sum_{i=1}^{4} D_{si}, F_\theta = \sum_{i=1}^{4} M_{si} &+ \frac{B}{\sqrt{2}}(L_{s1} - D_{s2} - L_{s3} + D_{s4})\cos\left(\frac{\pi}{4}+\theta\right) \\ &+ \frac{B}{\sqrt{2}}(D_{s1} + L_{s2} - D_{s3} - L_{s4})\sin\left(\frac{\pi}{4}+\theta\right), \end{aligned} \tag{5}$$

$$\begin{aligned} L_{si} &= \frac{1}{2}\rho U_{ri}^2 D(C_{Li}(\alpha_{ri})\cos\phi_{ri} + C_{Di}(\alpha_{ri})\sin\phi_{ri}), \\ D_{si} &= \frac{1}{2}\rho U_{ri}^2 D(-C_{Li}(\alpha_{ri})\sin\phi_{ri} + C_{Di}(\alpha_{ri})\cos\phi_{ri}), \\ M_{si} &= \frac{1}{2}\rho U_{ri}^2 D^2 C_{Mi}(\alpha_{ri}), \end{aligned} \tag{6}$$

$$\begin{aligned} &\alpha_{ri} = \theta + \phi_{ri},\ \phi_{ri} = \tan^{-1}\left(\frac{U_{yi}}{U_{zi}}\right),\ U_{ri} = \sqrt{{U_{yi}}^2 + {U_{zi}}^2}, \\ &U_{y1} = -\dot{y} - \frac{B}{\sqrt{2}}\dot{\theta}\cos\left(\frac{\pi}{4}+\theta\right),\ U_{z1} = U - \dot{z} - \frac{B}{\sqrt{2}}\dot{\theta}\sin\left(\frac{\pi}{4}+\theta\right), \\ &U_{y2} = -\dot{y} - \frac{B}{\sqrt{2}}\dot{\theta}\sin\left(\frac{\pi}{4}+\theta\right),\ U_{z2} = U - \dot{z} + \frac{B}{\sqrt{2}}\dot{\theta}\cos\left(\frac{\pi}{4}+\theta\right), \\ &U_{y3} = -\dot{y} + \frac{B}{\sqrt{2}}\dot{\theta}\cos\left(\frac{\pi}{4}+\theta\right),\ U_{z3} = U - \dot{z} + \frac{B}{\sqrt{2}}\dot{\theta}\sin\left(\frac{\pi}{4}+\theta\right), \\ &U_{y4} = -\dot{y} + \frac{B}{\sqrt{2}}\dot{\theta}\sin\left(\frac{\pi}{4}+\theta\right),\ U_{z4} = U - \dot{z} - \frac{B}{\sqrt{2}}\dot{\theta}\cos\left(\frac{\pi}{4}+\theta\right). \end{aligned} \tag{7}$$

When the four-bundled conductor exhibits torsional velocity, each sub-conductor will gain velocity in the circumferential direction. Therefore, the relative angle of attack, α_{ri}, and relative wind speed, U_{ri}, for each sub-conductor $(i = 1\text{–}4)$ are functions of torsional velocity, $\dot{\theta}$. By formulating the quasi-steady aerodynamic forces in this way, the aerodynamic forces caused by the torsional velocity can be included. Additionally, the relative angle of attack, α_r, and relative wind speed, U_r, for the whole four-bundled conductor are derived as follows:

$$\alpha_r = \theta + \phi_r,\ \phi_r = \tan^{-1}\left(\frac{-\dot{y}}{U - \dot{z}}\right),\ U_r = \sqrt{(-\dot{y})^2 + (U - \dot{z})^2}. \tag{8}$$

When the torsional motion is not considered, the total aerodynamic forces calculated from each sub-conductor independently, using Eq. (7) and C_{Di}, C_{Li} $(i = 1–4)$, are the same as those calculated for the whole bundled conductor using Eq. (8) and C_{Df}, C_{Lf}.

2.3 Numerical analysis method

Time–history analysis was performed using the fourth-order Runge–Kutta method by varying the setup torsional angle, θ_0, DoFs, and frequency ratios at a constant wind speed. First, the stationary position and orientation of the conductor with respect to the wind, whose displacements in the vertical, horizontal, and torsional directions are y_s, z_s, and θ_s, respectively, are calculated from the time-history analysis with large virtual damping. Then, the displacements at the first time-step of the dynamic analysis with the more realistic damping from Table 1 are set as $(y_{t=0}, z_{t=0}, \theta_{t=0}) = (y_s + \Delta_{y0}, z_s + \Delta_{z0}\ , \theta_s + \Delta_{\theta 0})$. An initial displacement was applied only to the vertical displacement, Δ_{y0}, which was set at a series of values from 0.0 to 5.0 m in intervals of 0.05 m. In contrast, initial displacements in the horizontal and torsional direction, Δ_{z0} and $\Delta_{\theta 0}$, and initial velocities of every direction were zero.

The response amplitudes, phase differences between the displacements, and frequencies were obtained from the time–history analyses when the amplitudes reached a steady state. The time step in this analysis was 0.02 s, and the total time taken, which varies with the stationarity of oscillations, was longer than 600 s. In this study, the amplitude is defined as a value that is half of the peak-to-peak amplitude. The phase difference between the two motions was calculated from the time difference of the zero crossing-points of displacement and with positive velocity. The frequency was calculated from the time period between the zero crossing-points. In a few cases of small amplitude, the response did not reach a full steady-state oscillation. In these cases, the response characteristics were described by the ensemble average of each parameter from the last 120 s.

3. Characteristics of vertical 1-DoF non-linear oscillations

In this section, the characteristics of the non-linear oscillation caused by the non-linear aerodynamic forces are described using the results of time–history analysis of the vertical 1-DoF system. The relationship between the relative angle of attack and the work done by the aerodynamic force was considered to describe the oscillation mechanism. Then, the characteristics of stable and unstable limit-cycle oscillation amplitudes were clarified by factoring in the energy balance of vertical motion over one oscillation period.

3.1 Excitation mechanism of vertical 1-DoF oscillation

Figure 4 illustrates the relationship between the torsional angle, $\theta_0(=\theta_s)$, and the vertical amplitude obtained from the vertical 1-DoF analysis, in which the initial value of the vertical displacement, Δ_{y0}, was 5 m. The absolute value of the Den Hartog summation (Fig. 3) at the torsional angle does not correlate well with the amplitude. The largest amplitude was observed when the torsional angle, θ_0, was 58°, which is outside the angle range required to fulfil the Den Hartog criterion. Furthermore, Fig. 4 shows the range of the relative angle of attack, α_r, during the oscillations and value of the lift coefficient for reference. The range of α_r for $\theta_0 = 20\text{–}38, 48\text{–}58°$ includes the range of angles in which the lift coefficient exhibited a large negative slope (20-

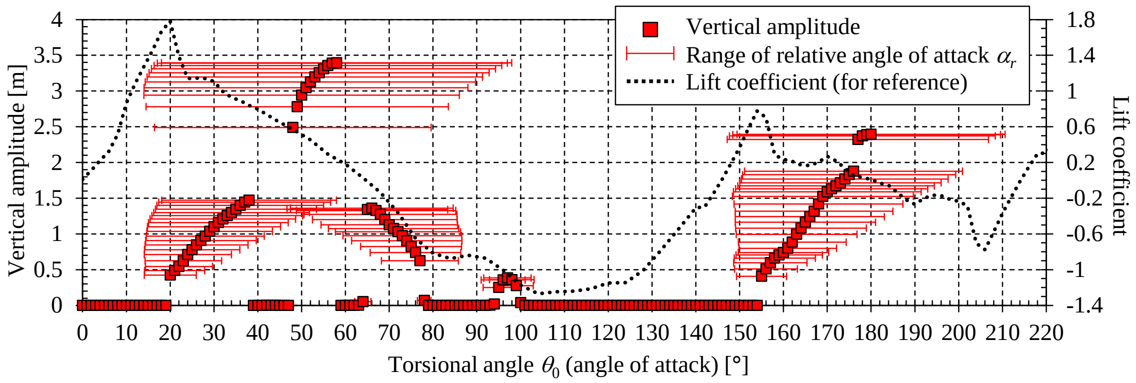

Fig. 4 Relationship between torsional angle and vertical amplitude with range of relative angle of attack (results of time–history analysis for the vertical 1-DoF system with initial displacement $\Delta y_0 = 5$ m)

25°). The cause of the large oscillations and the reason for the sudden changes in amplitudes in relation to the torsional angle were investigated by focusing on the work done by the aerodynamic force in the following.

During vertical 1-DoF oscillation, aerodynamic force F_y, relative wind speed U_r and relative angles of attack α_r are expressed as follows:

$$F_y = \frac{1}{2}\rho U_r^2 4D\big(C_{Lf}(\alpha_r)\cos\phi_r + C_{Df}(\alpha_r)\sin\phi_r\big), U_r = \sqrt{U^2 + \dot{y}^2}, \alpha_r = \theta_0 + \tan^{-1}\left(\frac{-\dot{y}}{U}\right). \quad (9)$$

When the response displacement approximates a sine wave, the energy balance over one period, T, is obtained as follows:

$$E_T = \int_{-\frac{T}{2}}^{\frac{T}{2}} \left(F_y\dot{y} - 2m\zeta_{y0}\omega_{y0}\dot{y}^2\right)\mathrm{d}t \approx \int_{-\frac{T}{2}}^{\frac{T}{2}} \left(\tilde{F}_y\dot{y} - 2m\zeta_{y0}\omega_{y0}\dot{y}^2\right)\mathrm{d}t. \quad (10)$$

The first term corresponds to the work done by the aerodynamic force, and the second term corresponds to that of the structural damping force. $\tilde{F}_y$ is the dynamic component of the aerodynamic force in the vertical direction, given by F_y minus its time-averaged value. At a certain time, when the power $\tilde{F}_y\dot{y} > 0$, the fluctuating aerodynamic force in the vertical direction, $\tilde{F}_y$, promotes oscillation. However, when power $\tilde{F}_y\dot{y} < 0$, $\tilde{F}_y$ suppresses oscillation.

Figure 5 demonstrates the time-series of vertical velocity, $\dot{y}$, relative angles of attack, α_r, and the variation of the aerodynamic force in the vertical direction, $\tilde{F}_y$, at $\theta_0 = 38$ and $58°$. By considering the relationship between $\dot{y}$ and α_r, the oscillation is excited by the fluctuating aerodynamic force when $\tilde{F}_y > 0$ in the region where the relative angle of attack, α_r, is smaller than the torsional angle, θ_0, or when $\tilde{F}_y < 0$ in the region where α_r is larger than θ_0. Figure 5 also shows the time when oscillation is considerably excited by the fluctuating aerodynamic force when α_r reaches the area around the stalling angle (20°) because both $\dot{y}$ and $\tilde{F}_y$ have large absolute values with the same sign. Furthermore, in the case of $\theta_0 = 58°$ (Fig. 5 (b)) , the

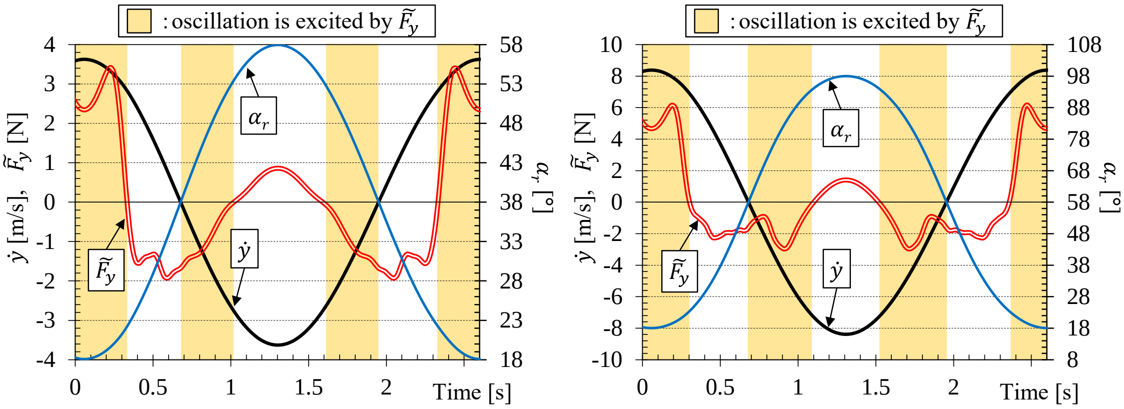

(a) $\theta_0 = 38°$ (b) $\theta_0 = 58°$

Fig. 5 Time series of each parameter (vertical 1-DoF system)

oscillation is also excited when the range of α_r includes the angle range in which there is a bulge in the lift coefficient around 80°.

Similarly, the large oscillation seems to be caused by the range of the relative angle of attack, including the angle range with steep negative slopes for the lift coefficient of approximately 20–25°, 70–80°, and 150–160°. The range of the relative angle of attack changes according to the oscillation amplitude. The cause of the large oscillation can be determined by analysing the relationship between the relative angle of attack and the work performed by aerodynamic forces at a given time, as mentioned previously.

3.2 Characteristics of stable and unstable limit-cycle oscillation amplitudes

Figure 6 compares the vertical amplitude at each torsional angle, $\theta_0 (= \theta_s)$, obtained from the vertical 1-DoF

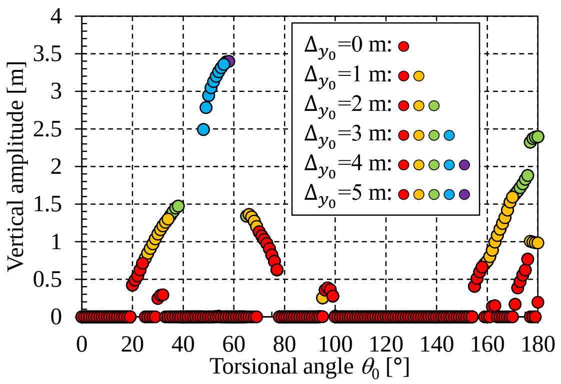

Fig. 6 Dependency of initial displacement on the vertical amplitude for the vertical 1-DoF system (results of time–history analysis, with initial displacement Δy_0 = 0, 1, 2, 3, 4, and 5 m)

analysis, in which the initial value of vertical displacement, Δ_{y0}, is 0, 1, 2, 3, 4, and 5 m. For some torsional angles, galloping was observed only when the initial displacement was larger than a certain value. In other words, this system had an unstable limit cycle. Stable and unstable limit-cycle oscillations are typical characteristics of a non-linear oscillator. They are caused by non-linear aerodynamic forces in this case. These characteristics are also observed for a square prism, as described by Parkinson and Smith (1964) and Novak (1969, 1972). Next, all stable limit-cycle-oscillation amplitudes were selected from steady-state solutions obtained through time-history analysis with all initial displacements of $\Delta_{y0} = 0.0\text{–}5.0$ m (intervals of 0.05 m). Meanwhile, the unstable limit-cycle-oscillation amplitude is defined as the minimum initial displacement, Δ_{y0}, that is necessary to obtain the corresponding stable limit-cycle oscillation. The description of the characteristics of stable and unstable limit-cycle-oscillation amplitudes and the relevant estimation method are as follows.

If the vertical displacement is assumed to be $y = \bar{y} + A_y \sin \omega_G t$, where ω_G is the circular frequency of the galloping oscillations, the steady-state solutions (A_y and ω_G) can be obtained from two equations: the time integral of the multiplication of y on both sides of the equation of motion (the first part of Eq. (4)) and the time integral of the multiplication of $\dot{y}$ by the same. The former equation is shown as follows:

$$f_{ys} = \int_{-\frac{T}{2}}^{\frac{T}{2}} \left(F_y \cdot A_y \sin \omega_G t\right) \, \mathrm{d}t - m\left(\omega_{y0}^2 - \omega_G^2\right) \frac{A_y^2}{\omega_G} \pi = 0. \tag{11}$$

When the vertical displacement is $y = \bar{y} + A_y \sin \omega_G t$, and the vertical velocity is $\dot{y} = A_y \omega_G \cos \omega_G t$. Based on Eq. (9), the aerodynamic force is an even function of t. That is, $F_y(-t) = F_y(t)$. From this, the integral term in Eq. (11) is zero, and the oscillation frequency $\omega_G = \omega_{y0}$.

Meanwhile, the latter equation corresponds to E_T from Eq. (10),which equals zero. Therefore, the steady-state vertical amplitude, A_y, for both stable and unstable solutions can be estimated with $E_T = 0$ and $\omega_G = \omega_{y0}$. In other words, when the oscillation reaches a steady state, the energy input from work done by the

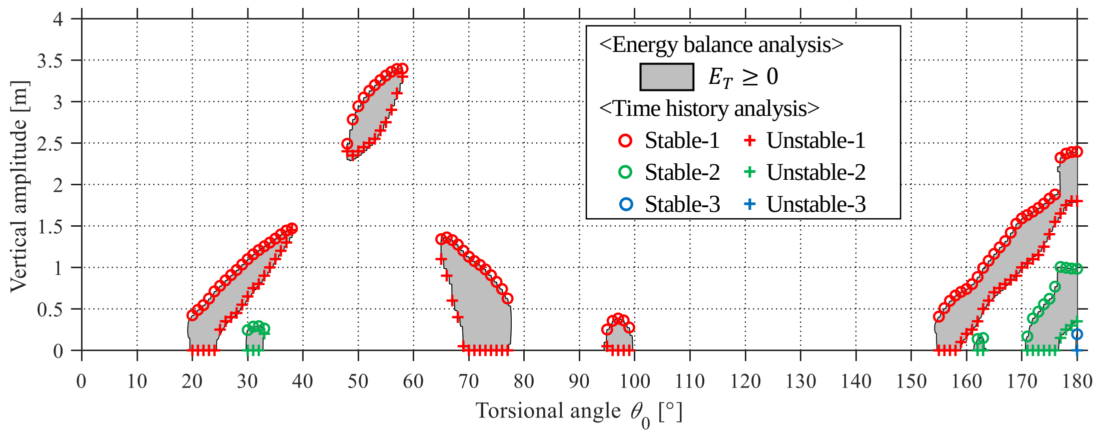

Fig. 7 Comparison of stable and unstable limit-cycle amplitudes between time-history analysis and energy-balance analysis for the vertical 1-DoF system

aerodynamic force is balanced by the energy output of the structural damping force over each period, and $E_T = 0$. When $E_T > 0$, the oscillation amplitude becomes larger than the assigned vertical amplitude, A_y, whereas $E_T < 0$ indicates that the oscillation amplitude becomes smaller than the assigned value.

Figure 7 compares the stable and unstable amplitudes obtained from the time–history analysis and the results of the energy-balance analysis. For energy-balance analysis, at each torsional angle, the range of amplitude, A_y, for which $E_T \geq 0$, is calculated. The maximum value of A_y in the range of $E_T \geq 0$, where $E_T = 0$, at each torsional angle indicates the stable limit-cycle amplitude. It corresponds to the steady-state amplitude and closely agrees with the amplitude value obtained by the time–history analysis. Meanwhile, the minimum value of A_y is in the range of $E_T \geq 0$, where $E_T = 0$ at each torsional angle indicates the unstable limit-cycle amplitude. This amplitude corresponds to the minimum initial displacement that must be applied for the oscillation to occur and is in agreement with the amplitude obtained by time–history analysis.

The torsional angle ranges in which galloping occurs with zero unstable limit-cycle amplitude correspond to the angle ranges where the Den Hartog summation (Fig. 3) is less than a certain negative value proportional to the structural damping ($-m\zeta_{y0}\omega_{y0}/\rho DU \approx -0.25$), as shown in Eq. (3). Furthermore, for the torsional angle ranges in which there is no value of A_y with $E_T \geq 0$, steady-state oscillations do not occur regardless of the large initial displacement. By considering the relationship between the relative angle of attack and the work done by the aerodynamic force, the unstable limit-cycle oscillation amplitude is determined by identifying whether the relative angle of attack attaches with the angle in which the aerodynamic force provided significant positive work to the oscillation. Thus, the angle ranges with steep negative slopes for the lift coefficient of approximately 20–25°, 70–80°, and 150–160° are shown in Fig. 4.

3.3 Non-dimensional energy-balance formulation in vertical 1-DoF system

By substituting Eq. (7) and $\dot{y} = A_y \omega_{y0} \cos \omega_{y0} t$ into Eq. (10), the conditional expression of the energy balance, $E_T \geq 0$, can be rearranged into a non-dimensional form as follows:

$$E_T^* = E_a^* - \frac{S_c}{U^*} \geq 0,$$
$$E_a^* = \frac{U^*}{A_y^*} \int_{-\pi}^{\pi} \left\{ \left(C_{Lf}(\alpha_r) - C_{Df}(\alpha_r) \cdot \frac{A_y^*}{U^*} \cos \psi \right) \sqrt{1 + \left(\frac{A_y^*}{U^*} \right)^2 \cos^2 \psi} \right\} \cos \psi \ \mathrm{d}\psi , \tag{12}$$
$$\alpha_r = \theta_0 - \tan^{-1} \left(\frac{A_y^*}{U^*} \cos \psi \right), A_y^* = \frac{A_y}{A_l}, \quad U^* = \frac{U}{A_l \omega_{y0}}, \quad S_c = \frac{4\pi m \zeta_{y0}}{\rho {A_l}^2}, \quad A_l = 4D.$$

As shown in these equations, the non-dimensional amplitude, A_y^*, with $E_T \geq 0$ is defined as a function of non-dimensional wind speed, U^*, and the Scruton number, S_c. Furthermore, Eq. (12) indicates that, when S_c/U^* is relatively small, the limit-cycle-oscillation amplitudes are proportional to the wind speed and are inversely proportional to the natural frequency. This state is fulfilled when the non-dimensional wind speed is high or when the damping is small. This relationship is the same as the one described by Parkinson and Smith (1964), who approximated the aerodynamic force as a polynomial expression.

Figure 8 shows the relationship between the non-dimensional amplitude, $A_y^*/U^* (= A_y \omega_{y0}/U)$, and the non-dimensional aerodynamic work, E_a^*. The area of $E_a^* \geq S_c/U^*$ corresponds to the area of $E_T \geq 0$ in Fig. 7. The non-dimensional aerodynamic work, E_a^*, which presents the aerodynamic characteristics of the

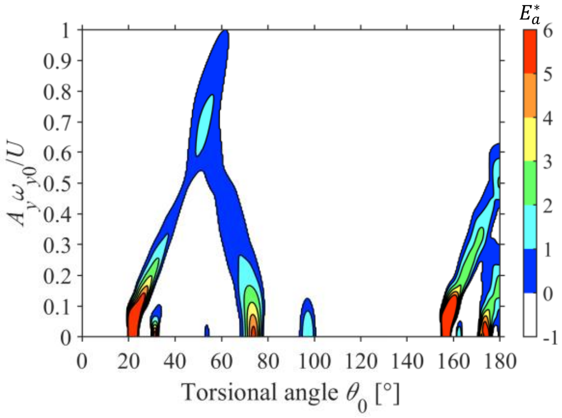

Fig. 8 Relationship between non-dimensional amplitude, A_y^*/U^*, and non-dimensional aerodynamic work, E_a^*, for the vertical 1-DoF system

section, can be calculated in advance, depending on the torsional angle. Therefore, by calculating S_c/U^*, the stable and unstable limit-cycle oscillation amplitudes for the vertical 1-DoF system can be easily estimated from Eq. (12) for various wind speeds and structural conditions. Furthermore, the amount of damping required to suppress the amplitude can be easily estimated. However, in the range of large non-dimensional aerodynamic work, it is hard to control galloping.

4. Aerodynamic coupling effect of 3-DoF galloping

To clarify the aerodynamic coupling effect of galloping of a four-bundled conductor, another series of time–history analyses was conducted for 2- and 3-DoF systems in addition to the vertical 1-DoF system. In this section, to discuss the tuning/de-tuning effect, which is the effect of the frequency ratio on the vertical amplitude, we first compared the results of the time–history analyses for vertical–horizontal–torsional 3-DoF systems with varying frequency ratios. Then, in the case with the largest amplitude of 3-DoF systems, the coupling characteristics and their mechanisms were investigated by comparing the results of the analysis for vertical–horizontal 2-DoF and vertical–torsional 2-DoF systems. Finally, the potential for the enlargement of the vertical amplitude by the horizontal and torsional motions was investigated by conducting a non-dimensional energy-balance analysis on the vertical motion, for which the horizontal and torsional amplitudes and their phase differences were assumed.

4.1 Effects of frequency ratio on stable limit-cycle-oscillation in 3-DoF systems

Figure 9 shows the dependency of the vertical amplitude on the torsional frequency ratio for the vertical–horizontal–torsional 3-DoF system. The vertical amplitude obtained from the analysis, in which only the frequency ratio between torsional and vertical motion was varied, was given as $f_{\theta 0}/f_{y0} = 0.7, 0.8, 0.9, 1.0, 1.1, 1.2, 1.3$ with the constant f_{y0}, f_{z0} $(= 0.393\ \text{Hz})$. In these figures, the horizontal axis represents the stationary torsional angle, θ_s, with wind, which was calculated from pre-time-history analysis with large virtual damping, and θ_s is different from the setup torsional angle, θ_0, in the case considering torsional motion. All different stable limit-cycle oscillation amplitudes were selected from the steady-state solutions obtained from the time-history analysis with all initial displacements, $\Delta_{y0} = 0.0\text{–}5.0$ m (intervals of 0.05 m), $\Delta_{z0} = 0$ m, and $\Delta_{\theta 0} = 0°$. Furthermore, these figures show the results of time-history analysis for a special case with an initial displacement of $\Delta_{y0} = 0$ m. In the 3-DoF system, stable limit-cycle oscillations occurred in a wider range of stationary torsional angles than torsional angles, $\theta_0 (= \theta_s)$, of the vertical 1-DoF analysis, as shown in Fig. 6. The torsional frequency ratio, $f_{\theta 0}/f_{y0}$, affects the conditions under which galloping occurs, as well as its amplitude. Larger galloping occurs in a wider range of stationary angles when the torsional natural frequency is smaller than the vertical natural frequency.

Figure 10 compares the vertical amplitudes between different torsional frequency ratios, $f_{\theta 0}/f_{y0} = 0.7, 0.8, 0.9, 1.0 (f_{z0} = f_{y0} = 0.393\ \text{Hz})$. In the range in which the stationary angle is approximately 40–90°, the vertical amplitude is affected by the torsional frequency ratio. The largest amplitude is observed at $f_{\theta 0}/f_{y0} = 0.9$ with some initial displacement, as shown in Fig. 10 (a). From Fig. 10 (b), in the case of

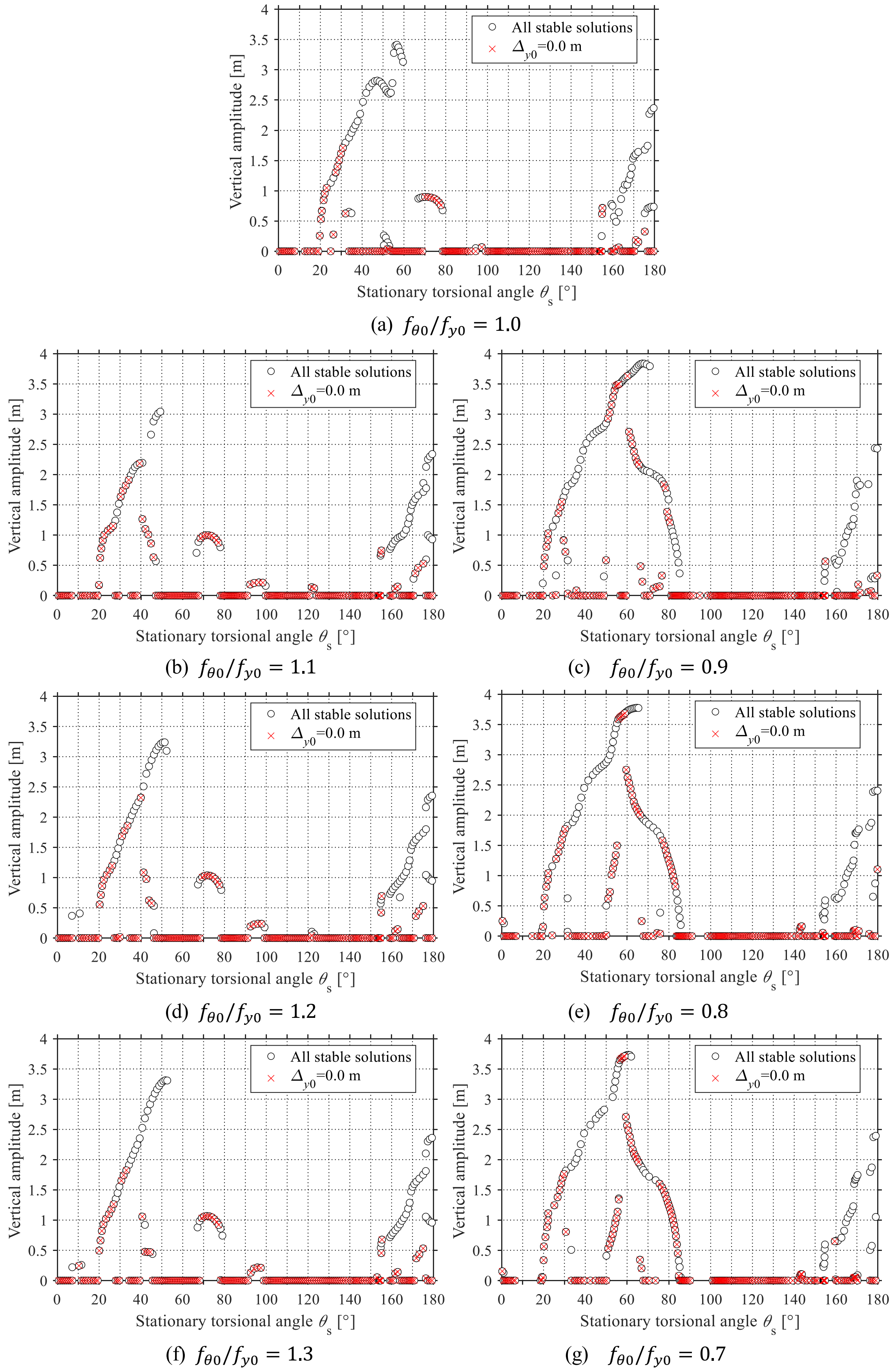

Fig. 9 Dependency of vertical amplitude on torsional frequency ratio for the 3-DoF system

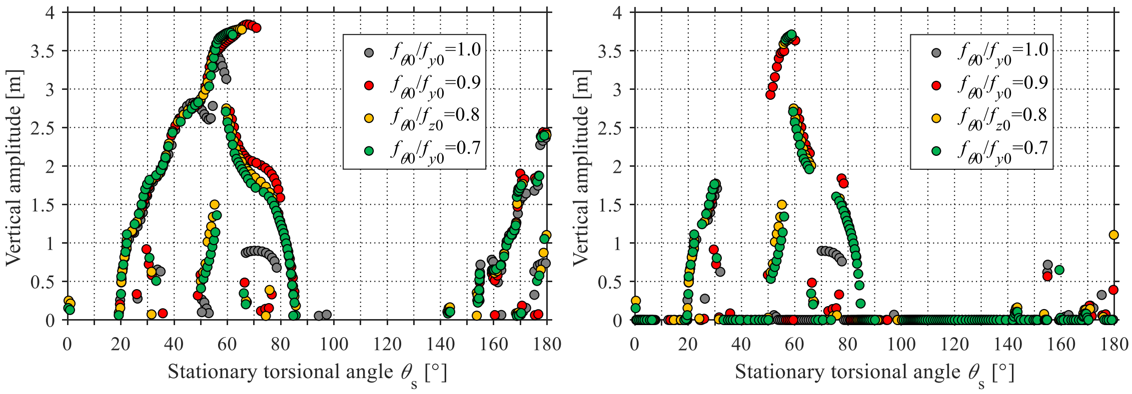

(a) All stable solutions larger than zero (b) Stable solutions in the case with $\Delta_{y0} = 0.0$ m

Fig. 10 Comparison of vertical amplitudes between different torsional frequency ratios for the 3-DoF system

$f_{\theta 0}/f_{y0} = 0.9$, large galloping is observed in the wider range of stationary torsional angles than for the other frequency ratio, even without initial displacement, $\Delta_{y0} = 0$ m. On the contrary, in the range of the other stationary torsional angle, where $\theta_s = 0–40$ and $90–180°$, the influence of torsional frequency ratio on the vertical amplitude is small: galloping occurs at $\theta_s = 20–40$ and $150–180°$, where galloping is also observed in the 1-DoF vertical systems.

Similarly, Fig. 11 compares the vertical amplitudes between different horizontal frequency ratios in the 3-DoF system, $f_{z0}/f_{y0} = 0.8, 0.9, 1.0, 1.1, 1.2$ ($f_{\theta 0} = f_{y0} = 0.393$ Hz). In the range in which the stationary angle is approximately 20–60°, the vertical amplitude is affected by the horizontal frequency ratio. In the case of $f_{z0}/f_{y0} = 1.0$, the amplitude is larger than those of the other frequency ratios. The stationary torsional range in which galloping occurs is narrower when the horizontal natural frequency ratio is larger than

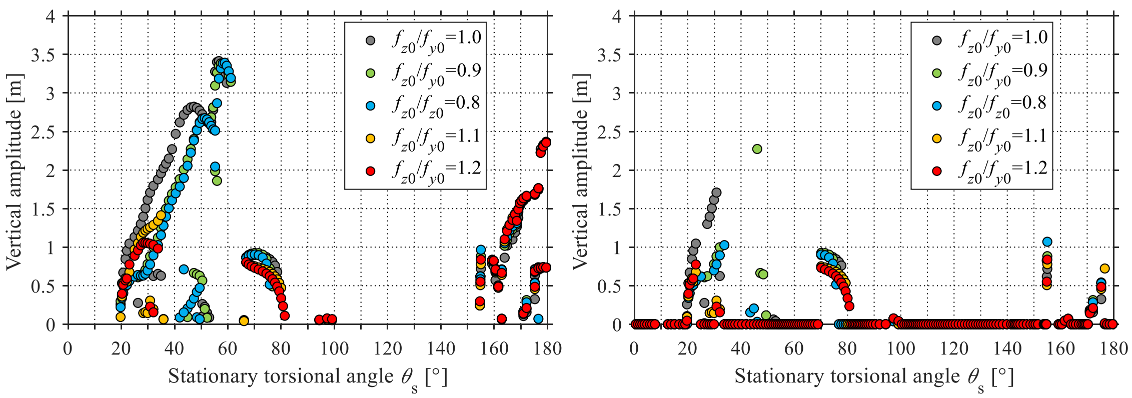

(a) All stable solutions larger than zero (b) Stable solutions in the case with $\Delta_{y0} = 0.0$ m

Fig. 11 Comparison of vertical amplitudes between different horizontal frequency ratios for the 3-DoF system

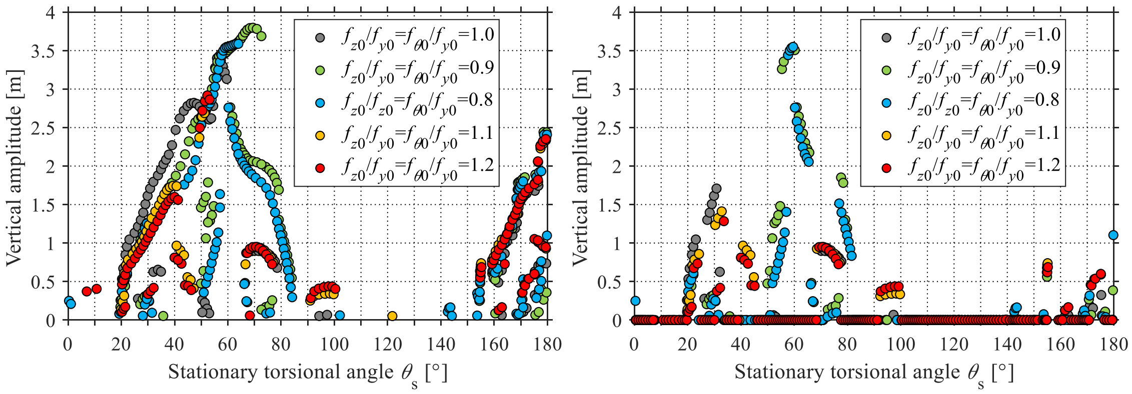

(a) All stable solutions larger than zero (b) Stable solutions in the case with $\Delta_{y0} = 0.0$ m

Fig. 12 Comparison of vertical amplitudes between different horizontal and torsional frequency ratios for the 3-DoF system

the vertical natural frequency than when $f_{z0}/f_{y0} = 1.0$. When the horizontal natural frequency ratio is smaller than the vertical natural frequency, the stationary torsional range in which galloping occurs is almost the same as that when $f_{z0}/f_{y0} = 1.0$. By contrast, in the stationary torsional angle range of $\theta_s = 150$– $180°$, where the 1-DoF vertical systems experience galloping, the effect of the horizontal frequency ratio on the vertical amplitude is small.

Finally, Fig. 12 shows differences in vertical amplitude of the 3-DoF system observed when both the horizontal–vertical and torsional–vertical frequency ratios were varied with a constant $f_{y0}(= 0.393$ Hz). From the results of the frequency-ratio variation in the 3-DoF system, as shown in Figs. 10, 11, and 12, the largest vertical amplitudes in the wide stational torsional angle range are observed in the case having $f_{z0}/f_{y0} = 1.0$ and $f_{\theta0}/f_{y0} = 0.9$.

4.2 Oscillation characteristics of 3-DoF galloping with $f_{z0}/f_{y0} = 1.0$, $f_{\theta0}/f_{y0} = 0.9$

Figure 13 illustrates the oscillation characteristics for the case having vertical amplitude, horizontal amplitude, torsional amplitude, amplitude of relative angle of attack, frequency of oscillation, phase difference between horizontal and vertical displacement, phase difference between torsional and vertical displacement, and phase

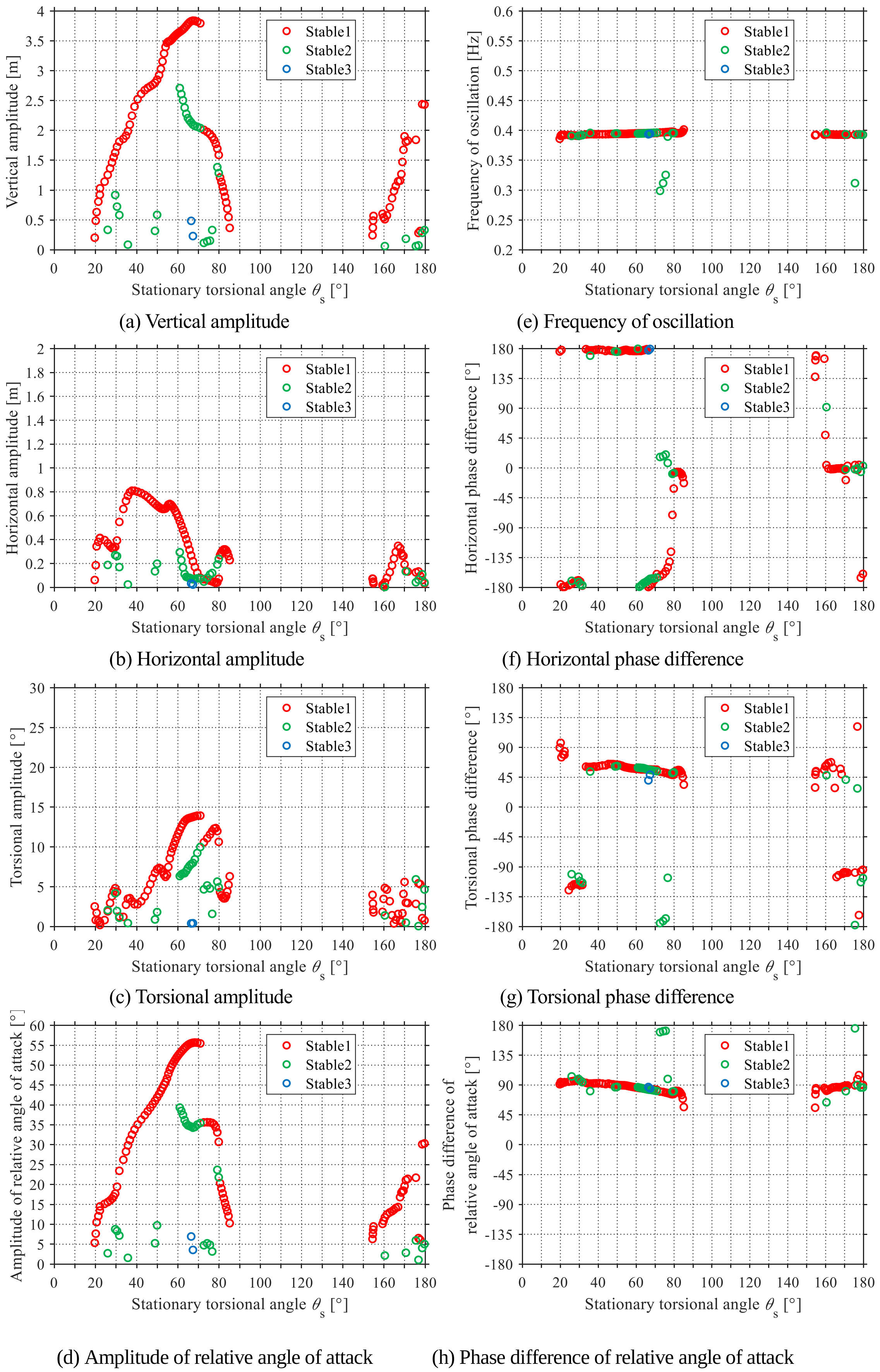

(a) Vertical amplitude (e) Frequency of oscillation

(b) Horizontal amplitude (f) Horizontal phase difference

(c) Torsional amplitude (g) Torsional phase difference

(d) Amplitude of relative angle of attack (h) Phase difference of relative angle of attack

Fig. 13 Oscillation characteristics of 3-DoF galloping ($f_{z0}/f_{y0} = 1.0$, $f_{\theta 0}/f_{y0} = 0.9$)

difference between the relative angle of attack, and the vertical displacement. Up to three different stable solutions were obtained from the time–history analysis for each torsional angle. The stable solutions are numbered in descending order of vertical amplitude for each torsional angle. In these figures, only those stable solutions having vertical amplitudes greater than 0.05 m are indicated. The relative angle of attack is not a sinusoidal wave, even if the vertical, horizontal, and torsional motions are substantially regarded as such. However, in this study, amplitude and phase difference of the relative angle of attack were defined the same as those of the displacements. That is, the amplitude of the relative angle of attack is defined as half of the peak-to-peak amplitude. Furthermore, the phase difference of the relative angle of attack is calculated by the time difference of the zero crossing-points of the relative angle of attack and the vertical displacement with positive velocity, respectively.

The frequency of oscillation is almost the same as the vertical natural frequency, except for a few cases. The largest vertical amplitude is approximately 4 m, whereas the largest horizontal amplitude is less than 1 m, and the largest torsional amplitude is approximately 15°. The horizontal and vertical displacements have almost opposite phases when the horizontal oscillation is relatively large (i.e., in the range $\theta_s = 20–70°$, where the horizontal amplitude is more than 0.4 m). Meanwhile, the torsional displacement is approximately 45–90° behind the vertical displacement when the torsional oscillation is relatively large (i.e., in the range $\theta_s = 30–90°$ where the torsional amplitude is more than 5°).

The amplitude of the relative angle of attack increases as the vertical amplitude increases. The phase of the relative angle of attack is approximately 90° behind the vertical displacement. In other words, the relative angle of attack is mainly determined by the effect of the vertical velocity. Based on these characteristics, the vertical oscillation is dominant, even in the 3-DoF galloping. Thus, the cause of large oscillations and coupling effects can be investigated by analysing the relationship between the relative angle of attack and the work done by the aerodynamic force in the vertical direction, as was done with the vertical 1-DoF system in Section 3.1. The oscillation mechanism and the effect of coupling on the 3-DoF galloping are described in the next section.

4.3 Fundamental characteristics of aerodynamic coupling in a 3-DoF system

Figure 14 compares the vertical amplitudes of all different stable solutions obtained from the time-history analyses for various DoF systems and frequency ratios with $f_{y0} = 0.393$ Hz: vertical–horizontal–torsional 3-DoF system with $f_{z0}/f_{y0} = 1.0, f_{\theta 0}/f_{y0} = 0.9$; vertical–horizontal 2-DoF system with $f_{z0}/f_{y0} = 1.0$; vertical–torsional 2-DoF system with $f_{\theta 0}/f_{y0} = 0.9$; and vertical 1-DoF system. The aerodynamic coupling

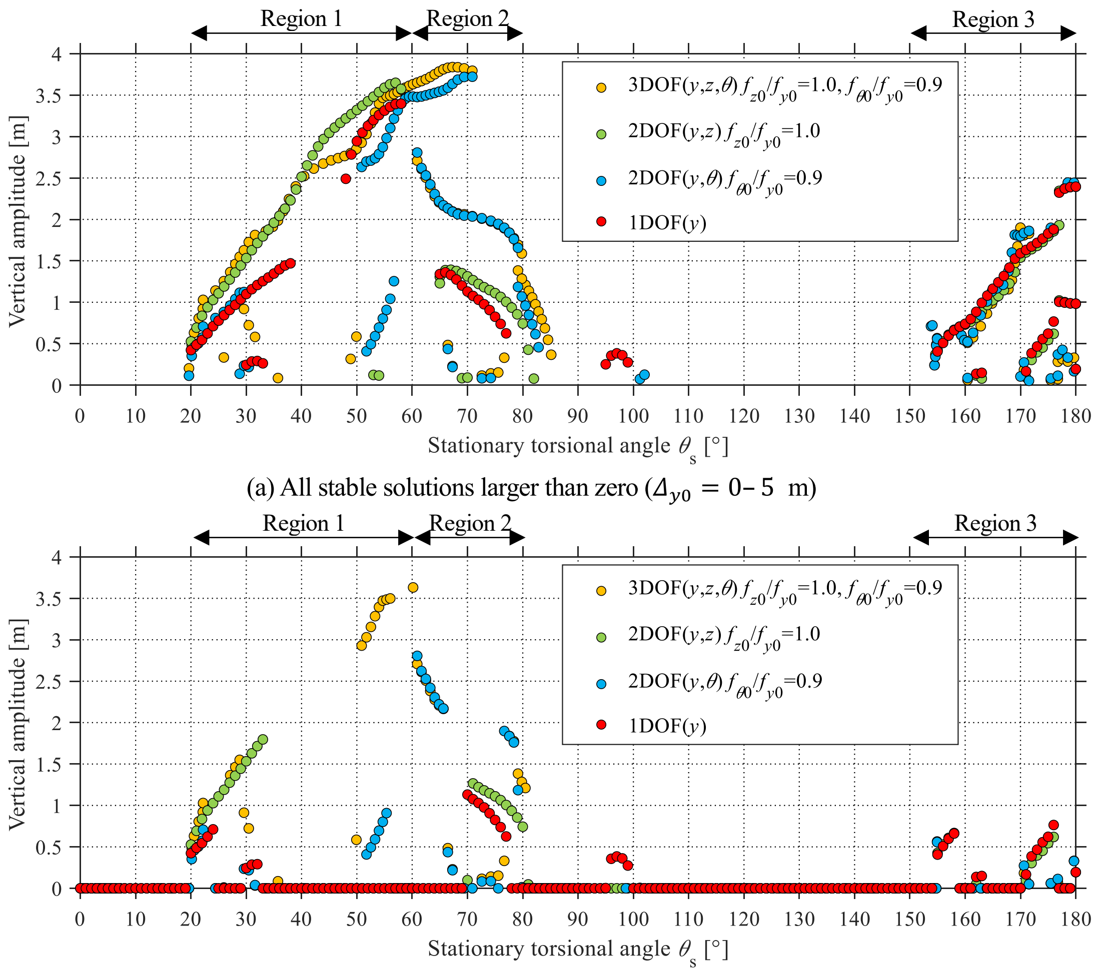

(a) All stable solutions larger than zero ($\Delta_{y0} = 0\text{–}5$ m)

(b) Stable solutions in the case with $\Delta_{y0} = 0.0$ m

Fig. 14 Comparison of vertical amplitudes under various DoF systems and frequency ratios (Time–history analysis, $\Delta_{y0} = 0\text{–}5$ m) effect between the motions can be clarified by accounting for the effect of each frequency ratio, as mentioned in Section 4.1, the amplitude of motion in each direction, as mentioned in Section 4.2, and the oscillation characteristics in 2-DoF systems, as shown in Fig. 14. Focusing on the largest amplitude of each stationary torsional angle, the stationary torsional angle can be partitioned into three regions based on the coupling effects as follows:

Region 1: The stationary torsional angle was approximately 20–60°. The results of the vertical–horizontal 2-DoF analysis ($f_{z0}/f_{y0} = 1.0$) approaches those of the 3-DoF analysis ($f_{z0}/f_{y0} = 1.0$) having larger amplitudes than the others for each stationary torsional angle. In this region, the vertical–horizontal 2-DoF coupling oscillation is dominant when both frequencies are equal.

Region 2: The stationary torsional angle was approximately 60–80°. The results of the vertical–torsional 2-DoF analysis ($f_{\theta 0}/f_{y0} = 0.9$) approach those of the 3-DoF analysis ($f_{\theta 0}/f_{y0} = 0.9$) with larger amplitudes than the others for each stationary torsional angle. In this region, the vertical–torsional 2-DoF coupling oscillation is dominant when the torsional frequency is slightly lower than the vertical frequency.

Region 3: The stationary torsional angle was approximately 150–180°. The results of all analyses are approximately equal. The vertical 1-DoF oscillation is dominant in this region.

The oscillation mechanism in Region 3 is simply described by the results of the vertical 1-DoF analysis, as mentioned in Section 3.1. Thus, the oscillation mechanism of Regions 1 and 2 is discussed using the results of the vertical–horizontal or vertical–torsional 2-DoF analysis, as follows.

In Region 1, the horizontal motion is coupled with the vertical motion and enlarges the vertical amplitude. Figure 15 shows the time series of each variable at a torsional angle of $\theta_0 = \theta_s = 56°$ in the vertical–horizontal 2-DoF analysis ($f_{z0}/f_{y0} = 1.0$). To clarify the influence of the horizontal motion, the relative angles of attack, α_r, relative wind speed, U_r, and the fluctuating aerodynamic force, $\widetilde{F_y}$, are compared

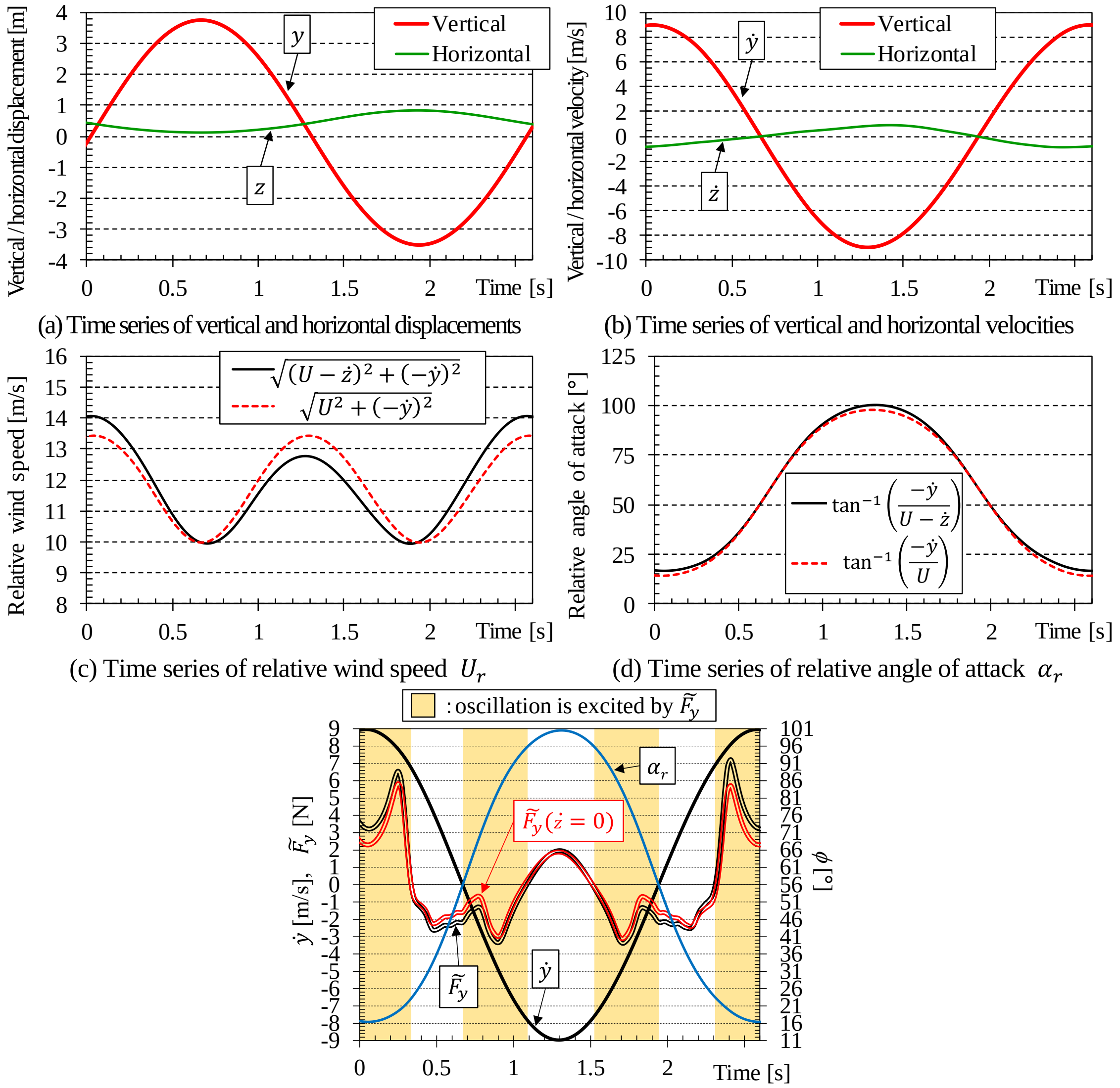

(a) Time series of vertical and horizontal displacements

(b) Time series of vertical and horizontal velocities

(c) Time series of relative wind speed U_r

(d) Time series of relative angle of attack α_r

(e) Time series of α_r, $\dot{y}$, $\widetilde{F}_y$ and $\widetilde{F}_y(\dot{z}=0)$

Fig. 15 Time series of each variable compared to those without horizontal velocity at torsional angle $\theta_0 = \theta_s = 56°$ (vertical–horizontal 2-DoF system, $f_{z0}/f_{y0} = 1.0$)

with those with a horizontal velocity of $\dot{z} = 0$ in Fig. 15. As shown in Fig. 15 (c), (d), the influence of the horizontal velocity is predominant in the relative wind speed. Because the phase difference between the vertical and horizontal motions is approximately 180°, the relative wind speed increases because of the horizontal velocity when the relative angle of attack is small. In contrast, the relative wind speed decreases when the relative angle of attack is large. As a result, from Fig. 15 (e), the fluctuating aerodynamic force increases at a time when the relative angle of attack is approximately 20°, and it exerts a larger exciting force than that where $\dot{z}$ = 0. This is the why the horizontal motion enlarges the vertical amplitude in Region 1.

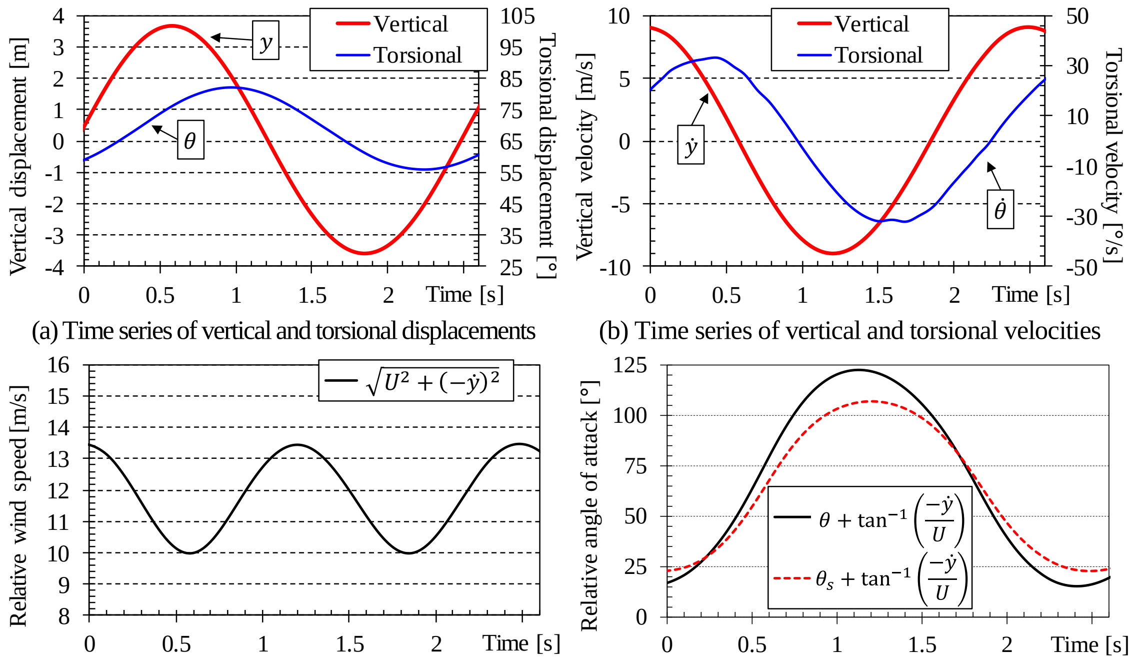

(a) Time series of vertical and torsional displacements

(b) Time series of vertical and torsional velocities

(c) Time series of relative wind speed

(d) Time series of relative angle of attack

Fig. 16 Time series of each variable compared to those without torsional displacement at setup torsional angle $\theta_0 = 65°$ (vertical–torsional 2-DoF system, $f_{\theta 0}/f_{y0} = 0.9$, stationary torsional angle $\theta_s = 67.3°$)

In Region 2, the torsional motion is coupled with the vertical motion and enlarges the vertical amplitude. Figure 16 shows the time series of each variable at the setup torsional angle of $\theta_0 = 65°$ in the vertical–torsional 2-DoF analysis ($f_{\theta 0}/f_{y0} = 0.9$). In the case where $\theta_0 = 65°$, the stationary torsional angle, θ_s, is 67.3°. To clarify the influence of torsional motion, the relative angles of attack, α_r, and relative wind speed, U_r, are compared with those with a torsional displacement of $\theta = \theta_s$ (constant) in Fig. 16. As shown in Fig. 16 (d), because the phase difference between the vertical and torsional motions is 45–90°, the range of the relative angle of attack increases because of torsional oscillation. Thus, the range of the relative angle of attack can include the angle region around 20°, in which the aerodynamic force has a large positive effect on the oscillation, although the range does not attach the angle region around 20° with $\theta = \theta_s$. This is the why the torsional motion enlarges the vertical amplitude in Region 2.

The essential oscillation types of stable solutions in 3-DoF systems have been categorised according to the stationary torsional angle, and the coupling effects on the vertical oscillation have been discussed by analysing their influence on the relative angle of attack and relative wind speed. Even when focusing on the occurrence conditions under which galloping occurs from the stationary position (Fig 14 (b)), which corresponds to the range of stationary angles having a negative damping effect in the linear analysis, the coupling effects on the occurrence conditions are similar to those on non-linear oscillation amplitudes. When $\theta_s = 20\text{–}40°$, the range in which galloping occurs for the 3-DoF system with $f_{z0}/f_{y0} = 1.0$ is almost the same as that in which galloping occurs for the vertical–horizontal 2-DoF system. For $\theta_s = 50\text{–}70°$, the range of galloping occurrence of the 3-DoF system with $f_{\theta 0}/f_{y0} = 0.9$ is almost the same as that of the vertical–torsional 2-DoF system, except that the amplitudes are different because there are multiple stable solutions. In $\theta_s = 150\text{–}180°$, the range in which galloping occurs in the 1-DoF system is the same or slightly wider than the range in which galloping occurs in the other systems. The coupling effect is also pronounced in the unstable limit-cycle oscillation amplitudes, which are the initial displacements necessary to induce the corresponding larger-amplitude stable solutions. Although the initial displacement in the time–history analysis was set only in the vertical direction, an unstable solution should be defined as a function of the displacement and velocity of every motion (i.e., a combination of their amplitudes and phases). The identification of unstable solutions in multiple DoF systems, which is a characteristic of non-linear vibrations, requires further investigation using the results of time–history analysis with various combinations of initial conditions or other theoretical non-linear dynamics approaches.

4.4. Enlargement of vertical amplitude with assumed horizonal and torsional oscillations

In Sections 4.1–4.3, the coupling effects of the 3-DoF galloping were investigated in a specific case, whose conditions are shown in Table 1. Under other structural and wind conditions, the horizontal and torsional oscillations might vary even for the same ice-accretion shape. To indicate more general characteristics for enlargement of the vertical amplitude by other motions, the maximum vertical amplitude in the presence of assumed horizontal and torsional oscillations was investigated using the non-dimensional energy-balance formulation for vertical vibrations. Hence, the conditions of horizontal and torsional oscillations under which the vertical vibrations were enlarged for the 3-DoF system were clarified. Even for a multi-DoF system, the relationship of energy balance over one period of time in the vertical direction, E_T, with the aerodynamic force in the vertical direction, F_y, is the same as that for a 1-DoF system, as shown in Eq. (10). However, the aerodynamic force, F_y, should be calculated using Eqs. (5), (6), and (7). Regarding the sinusoidal coupling motions in which the oscillation frequency is the same as the vertical natural frequency, the vertical, horizontal, and torsional displacements can be defined as $y = \bar{y} + A_y \sin \omega_{y0} t$, $z = \bar{z} + A_z \sin(\omega_{y0} t - \Phi_z)$, $\theta = \bar{\theta} + A_\theta \sin(\omega_{y0} t - \Phi_\theta)$, respectively. The amplitudes and phase differences are defined in a steady state in which the energy balance of each DoF of the multi-DoF system is established separately, and thus the steady-state oscillations shown in Fig 13 occur. Nevertheless, considering the energy balance only for the vertical motion and assuming the motions of the other DoFs (defined as four parameters: $A_z, \Phi_z, A_\theta, \Phi_\theta$), the largest vertical amplitude, A_y, that can occur for each mean torsional angle, $\bar{\theta}$, can be estimated from $E_T = 0$. Furthermore, the non-dimensional aerodynamic work for vertical oscillation coupling with horizontal and torsional oscillations, E_{ac}^*, can be expressed as follows:

$$E_{ac}^* = \frac{U^*}{A_y^*} \int_{-\pi}^{\pi} \left\{ \left(C_{Lf}(\alpha_r) \left(1 - \frac{A_y^*}{U^*} \frac{A_z}{A_y} \cos(\psi - \Phi_z) \right) - C_{Df}(\alpha_r) \frac{A_y^*}{U^*} \cos\psi \right) \times \sqrt{\left(1 - \frac{A_y^*}{U^*} \frac{A_z}{A_y} \cos(\psi - \Phi_z) \right)^2 + \left(\frac{A_y^*}{U^*} \right)^2 \cos^2 \psi} \right\} \cos\psi \ \mathrm{d}\psi,$$
$$\alpha_r = \bar{\theta} + A_\theta \sin(\psi - \Phi_\theta) - \tan^{-1} \left(\frac{\frac{A_y^*}{U^*} \cos\psi}{1 - \frac{A_y^*}{U^*} \frac{A_z}{A_y} \cos(\psi - \Phi_z)} \right). \quad (13)$$

Similarly, as in Fig. 8 using Eq. (12), the maximum value of A_y^*/U^* in the range of $E_{ac}^* - S_c/U^* \geq 0$ at each mean torsional angle, $\bar{\theta}$, corresponds to the largest non-dimensional vertical amplitude with assumed horizontal and torsional oscillations. As shown in Eq. (13), the non-dimensional amplitude, A_y^*/U^*, depends on the horizontal amplitude ratio, A_z/A_y; horizontal phase difference, Φ_z; torsional amplitude, A_θ; and torsional phase difference, Φ_θ; in addition to S_c/U^* at each mean torsional angle, $\bar{\theta}$. In the following, the effects of horizontal or torsional oscillations on the maximum vertical amplitudes are explained using the non-dimensional energy-balance formulation with assumed A_z/A_y and Φ_z or A_θ and Φ_θ, focusing on the vertical–horizontal 2-DoF system or the vertical–torsional 2-DoF system, respectively.

Figure 17 shows examples of the relationship between the non-dimensional amplitude, A_y^*/U^* $(= A_y\omega_{y0}/U)$, and the non-dimensional aerodynamic work, E_{ac}^*, for the vertical–horizontal 2-DoF systems with $A_z/A_y = 0.4, \Phi_z = 180°$ and for the vertical–torsional 2-DoF system with $A_\theta = 15°, \Phi_\theta = 60°$, respectively . The horizontal or torsional oscillation is assumed, referring to the galloping observed in Fig. 13. For conditions used in the time–history analyses, $S_c/U^* = 0.79$ and the largest non-dimensional vertical amplitude with assumed coupling oscillation can be estimated by the maximum value of A_y^*/U^* in the range of $E_{ac}^* \geq 0.79$. Compared with Fig. 8, which shows E_a^* in the vertical 1-DoF system, the boundaries for obtaining the stable solutions (upper boundary in the range of $E_{ac}^* - S_c/U^* \geq 0$) are affected by horizontal or torsional oscillation. When the structural damping is small or the non-dimensional wind speed is high, S_c/U^*

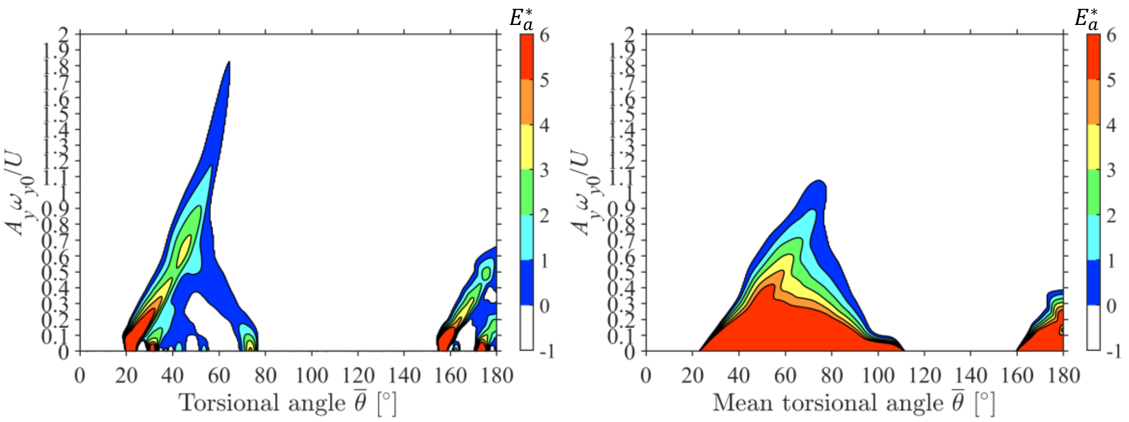

(a)Vertical–horizontal 2-DoF system
$(A_z/A_y = 0.4, \Phi_z = 180°, A_\theta = 0°)$

(b)Vertical–torsional 2-DoF system
$(A_\theta = 15°, \Phi_\theta = 60°, A_z/A_y = 0)$

Fig. 17 Relationship between non-dimensional amplitude, A_y^*/U^* $(= A_y\omega_{y0}/U)$, and non-dimensional aerodynamic work, E_a^*, for the vertical system

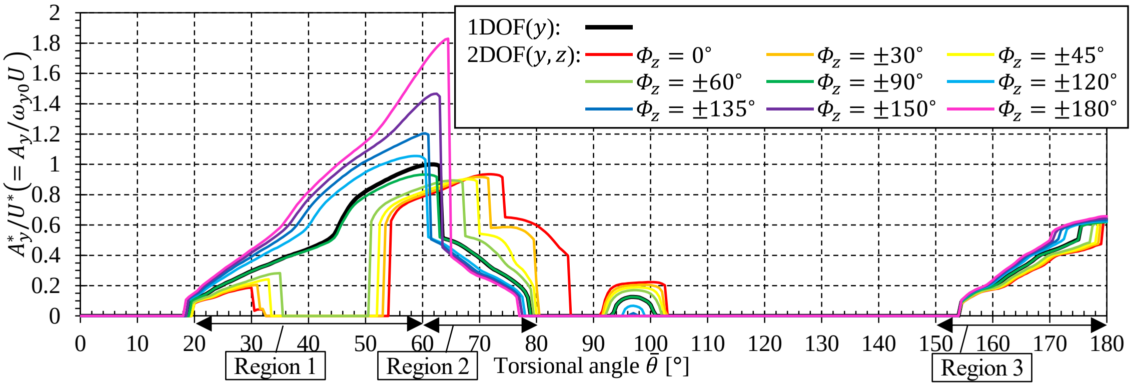

(a) Effect of horizontal phase difference Φ_z $(A_z/A_y = 0.4)$

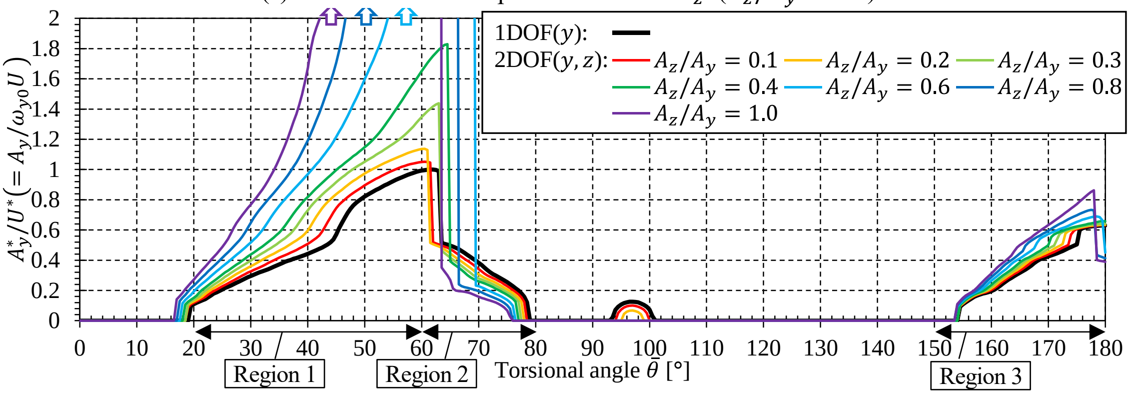

(b) Effect of amplitude ratio between horizontal and vertical oscillations A_z/A_y $(\Phi_z = 180°)$

Fig. 18 Effect of horizontal oscillation for the vertical–horizontal 2-DoF system (largest stable solutions of non-dimensional vertical amplitudes for each torsional angle, upper side of $E_{ac}^* \geq 0$)

becomes relatively small, and the potential largest vertical amplitude under assumed coupling oscillation can be estimated from the maximum value of A_y^*/U^* in the range of $E_{ac}^* \geq 0$. Because the non-dimensional potential amplitude, A_y^*/U^*, is calculated by using non-dimensional energy balance formulation, the potential largest vertical amplitude, A_y, can be easily estimated under various wind speeds and natural frequencies unless the effect of damping (S_c/U^*) is relatively large.

Figure 18 shows the effect of horizontal oscillation on the non-dimensional vertical amplitude for the vertical–horizontal 2-DoF system. These figures illustrate the largest stable limit-cycle oscillation amplitudes for each torsional angle obtained from the non-dimensional energy-balance analysis where $E_{ac}^* \geq 0$. Referring to the actual oscillation characteristic in multi-DoF galloping, as shown in Fig. 13, the non-dimensional vertical amplitudes with $A_z/A_y = 0.4$ (varying Φ_z) or $\Phi_z = 180°$ (varying A_z/A_y) are shown in these figures. As shown in Fig. 18 (a), the positive and negative horizontal phase differences have the same effect on the vertical

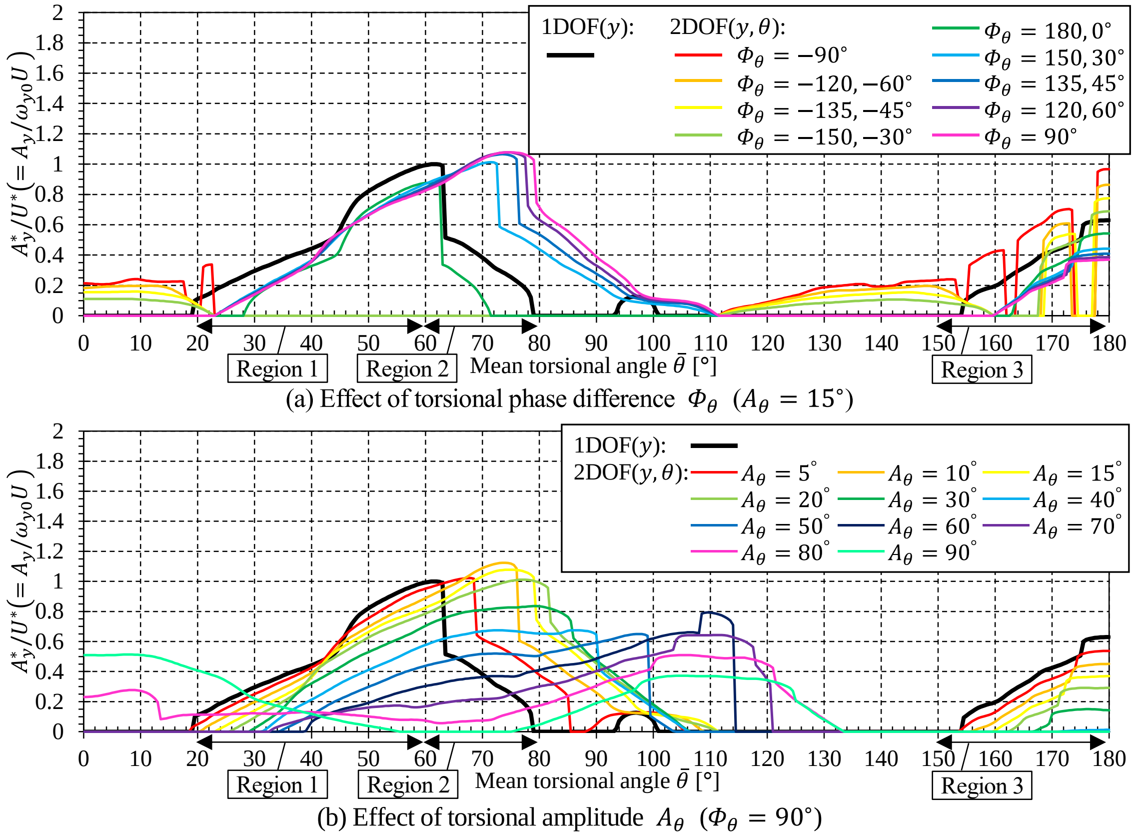

Fig. 19 Effect of torsional oscillation for the vertical–torsional 2-DoF system (largest stable solutions of non-dimensional vertical amplitudes for each mean torsional angle, upper side of $E_{ac}^{*} \geq 0$)

amplitude; only the absolute value of phase difference affects the vertical amplitude. For Region 1 ($\bar{\theta} =$ $20\text{–}60°$), where the dominant vertical–horizontal 2-DoF coupling oscillation is shown in time–history analysis, the vertical amplitude increases when the phase difference is greater than 90°; and a horizontal phase difference of 180° has the highest potential to enlarge the vertical amplitude. This is because the relative wind speed increases because of the horizontal velocity when the relative angle of attack is small, as mentioned in Section 4.3. As shown in Fig. 18 (b), under the condition of $\Phi_z = 180°$, the vertical amplitude could increase with the horizontal amplitude ratio, especially for that in Region 1 ($\bar{\theta} = 20\text{–}60°$).

Figure 19 illustrates the effect of torsional oscillation on the non-dimensional vertical amplitude for each mean torsional angle for the vertical–torsional 2-DoF system. The largest stable limit-cycle oscillation amplitudes for the vertical–torsional 2-DoF system are obtained from the non-dimensional energy-balance analysis wherein $E_{ac}^{*} \geq 0$, assuming the torsional amplitude, A_θ, and phase difference, Φ_θ, are independent of vertical motion. Referring to the actual oscillation characteristic in multi-DoF galloping, as shown in Fig. 13, the non-dimensional vertical amplitudes with $A_\theta = 15°$ (varying Φ_θ) or $\Phi_\theta = 90°$ (varying A_θ) are shown in these figures. From Fig. 19 (a), the torsional phase differences of $\Phi_\theta = 90° \pm \varphi$ are shown to have the same effect as the other on the vertical amplitude. For Region 2 ($\bar{\theta} = 60$– $80°$), where the dominant vertical–torsional 2-DoF coupling oscillation occurs in the time–history analysis, the range of the mean torsional angle in which the oscillations occur is widened as the phase difference approaches 90°. This is because the range of the relative angle of attack increases because of the torsional oscillation and reaches the angle range where the aerodynamic force has a large positive effect on the oscillation, as mentioned in Section 4.3. As shown in Fig. 19 (b), under the condition of $\Phi_\theta = 90°$, the range of the mean torsional angles, in which the oscillations occur, changes as the torsional amplitude increases. However, the vertical amplitude does not increase with an increasing torsional amplitude; it has a limited set of values, even if the torsional amplitude becomes large.

In summary, the vertical amplitude of multi-DoF galloping becomes larger with increasing horizontal amplitude (ratio) when the phase difference between the horizontal and vertical displacements is around 180°. In contrast, torsional oscillations can lead to multi-DoF galloping with the largest vertical amplitudes when the phase difference between the torsional and vertical displacements is around 90°. However, the maximum vertical amplitude is not significantly increased, even if the torsional amplitude becomes large. Note that the assumed amplitude (ratio) and phase difference for horizontal or torsional oscillations in Figs. 18 and 19 seem to include conditions that cannot be observed in the galloping of the ice-accreted four-bundled conductor. However, the conditions of amplitudes and phase differences of horizontal and torsional oscillation at which the vertical amplitude tends to increase are clarified from these figures. By identifying the structural conditions that induce a coupling effect which have those amplitudes and phase differences, it is possible to predict the conditions under which large galloping occurs.

5. Conclusions

To clarify the dynamic response characteristics of a four-bundled conductor to galloping, a series of time–history analyses were conducted for vertical 1-DoF, vertical–horizontal 2-DoF, vertical–torsional 2-DoF, and vertical–horizontal–torsional 3-DoF systems by formulating the quasi-steady aerodynamic forces for each sub-conductor. Then, the reasons for the large oscillations were deduced by analysing the relationship between the relative angle of attack and the work done by the aerodynamic force.

In the vertical 1-DoF system, the absolute value of the Den Hartog criterion at a given torsional angle did not correlate well with the oscillation amplitude. Large oscillations occurred because of the range of the relative angle of attack over the vibration cycle, including an angle range with a large negative slope of the lift coefficient. By considering the energy balance over one oscillation period, the stable and unstable limit-cycle amplitudes were identified and interpreted. By considering the relationship between the relative angle of attack and the work done by the aerodynamic force, the unstable limit-cycle oscillation amplitude was determined by identifying whether the relative angle of attack reattaches the angle at which the aerodynamic force had a positive effect on oscillation. Furthermore, the energy balance of the vertical motion over one oscillation period was evaluated using a function of the non-dimensional amplitude, non-dimensional wind speed, and the Scruton number. Using this non-dimensional formulation, the non-dimensional aerodynamic work, which presented the aerodynamic characteristics of the section, was calculated in advance for a given torsional angle. Subsequently, the stable and unstable limit-cycle oscillation amplitudes of the vertical 1-DoF system were easily estimated for various wind speeds and structural conditions, including damping and natural frequency.

The coupling effects of the horizontal and torsional motions on vertical oscillation amplitudes were observed for the 2- and 3-DoF systems, respectively. The essential oscillation types in the 3-DoF systems were categorised as vertical–horizontal 2-DoF coupled oscillations, vertical–torsional 2-DoF coupled oscillations, and vertical 1-DoF oscillations for different stationary torsional angles. The mechanisms of the coupling effects on the vertical oscillations, which enlarged the amplitude, were discussed by analysing their influence on the relative angle of attack and the relative wind speed. Finally, the coupling effects on the vertical oscillation were clarified by considering the non-dimensional energy balance of vertical motion with the prescribed amplitudes and phase differences of horizontal and torsional oscillations. The non-dimensional vertical amplitude for multi-DoF motion depends on the horizontal amplitude ratio and phase difference to the vertical oscillations and the torsional amplitude and torsional phase difference to the vertical oscillations, in addition to the non-dimensional wind speed and the Scruton number at each mean torsional angle. Thus, we conclude that the vertical amplitude of multi-DoF galloping can become large, apparently without limits, if the horizontal amplitude increases when the phase difference between the horizontal and vertical displacements is around 180°. In contrast, torsional oscillations can induce multi-DoF galloping with significant vertical amplitudes over a wider mean torsional angle range, when the phase difference between the torsional and vertical displacements approaches 90°; however, without horizontal motion, the vertical amplitude is limited, even if the torsional amplitude becomes large.

Although the fundamental effects of aerodynamic coupling and non-linearity on the oscillation amplitude of the conductor galloping are presented in this work, the time–history analyses were performed on a specific structural model and under a certain wind speed. Because the results of non-dimensional energy-balance analysis have also been presented, stable and unstable limit-cycle amplitudes of the vertical 1-DoF system can be obtained for various wind speeds and structural conditions. Furthermore, the mechanisms for enlarging the vertical amplitude for both the vertical 1-DoF and multi-DoF systems, which are explained by the influence of the relative angle of attack and relative wind speed, are applicable for various conditions. However, although the vertical amplitude for a multi-DoF system can be estimated when the amplitudes and phase differences of horizontal and torsional oscillation are assumed, the amplitudes and phase differences of these motions are defined in a steady state in which the energy balance for each motion is established separately, which has not been addressed in this paper. Therefore, it is necessary to perform further time–history analyses and discussions similar to those in this study by changing various parameters, including wind speed, structural conditions, and ice-accretion shape. Furthermore, we plan to develop another analytical evaluation method to obtain complete steady-state solutions, which includes the amplitude and phase differences of all motions, for non-linear coupled oscillation without using time–history analysis. Using the other evaluation method, we can obtain not only stable solutions but also unstable solutions in the multi-DoF system. In addition, the investigation should be expanded to a full-scale 3D model considering the distribution of responses. Eventually, after the verification of analytical results and theoretical description using experimental results for the 2D model and observation results for the 3D model, we plan to develop an evaluation method of steady-state galloping amplitudes for a multi-DoF 3D full-scale model of overhead transmission lines.

Acknowledgements

The authors are grateful to Dr. Takashi Nishihara (Central Research Institute of Electric Power Industry) for suggesting the topic addressed in this study and for helpful discussions on the mechanisms of non-linear oscillations.

References

Blevins, R., Iwan, W., 1974. The galloping response of a two-degree-of-freedom system. J. Appl. Mech., 41(4), 1113–1118.

CIGRE, 2007. State of the art of conductor galloping, CIGRE Technical Brochure, No. 322, TF B2.11.O6.

Den Hartog, J.P., 1956. Mechanical Vibrations, McGraw-Hill, New York.

Desai, Y. M., Shah, A.H. , Popplewell, N., 1990. Galloping analysis for two-degree-of-freedom oscillator. J. Eng. Mech., 10.1061/(ASCE)0733-9399(1990)116:12(2583), 2583–2602.

Desai, Y.M., Yu, P., Shah A.H., Popplewell, N., 1996. Perturbation-based finite element analysis of transmission line galloping. J. Sound Vib. 191, 469–489. https://doi.org/10.1006/jsvi.1996.0135.

He, M., Macdonald J.H.G., 2016. An analytical solution for the galloping stability of a 3 degree-of-freedom system based on quasi-steady theory. J. Fluid. Str. 60, 23–26. https://doi.org/10.1016/j.jfluidstructs.2015.10.004.

Jones, K.F., 1992. Coupled vertical and horizontal galloping. J. Eng. Mech. 118, 92–107. https://doi.org/10.1061/(ASCE)0733-9399(1992)118:1(92).

Kimura, K., Tanaka, N., Fujino, T., Yukino, T., Inoue, H., 1998. Wind tunnel and analytical study on a section model of ice-accreted 4 bundled conductor transmission lines. Proc. 6th East Asia-Pacific Conf. Struct. Eng. Constr., Taipei, Taiwan, 2293–2298.

Liu, X., Yan, B., Zhang, H., Zhou, S., 2009. Nonlinear numerical simulation method for galloping of iced conductor. Appl. Math. Mech. 30(4), 489–501. https://doi.org/10.1007/s10483-009-0409-x.

Lou, W., Wu, D., Xu, H., Yu, J., 2020. Galloping Stability Criterion for 3-DOF Coupled Motion of an Ice-Accreted Conductor. Journal of Structural Engineering 1;146(5):04020071.

Matsumiya, H., Ichikawa, H., Aso, T., Shugo, M., Nishihara, T., Shimizu, M., 2019. Galloping on single-conductor transmission lines with wet-snow accretion. Proc. 15th Int. Conf. Wind Eng., Beijing, China, 269-270.

Matsumiya, H., Nishihara, T., Shimizu, M., 2011. Aerodynamic characteristics of ice and snow accreted conductors of overhead transmission lines. Proc. 13th Int. Conf. Wind Eng., Amsterdam, Netherlands.

Matsumiya, H., Nishihara, T., Shimizu, M., Yukino, T., 2012. Observation of galloping of four-bundled conductors on ice-accreted overhead transmission lines. Proc. 2012 Int. Conf. Adv. Wind Struct., Seoul, Korea, 1238–1247.

Matsumiya, H., Nishihara, T., Yagi, T., 2018. Aerodynamic modeling for large-amplitude galloping of four-bundled conductors. J. Fluids Str. 82, 559–576. https://doi.org/10.1016/j.jfluidstructs.2018.08.003.

Morishita, S., Tsujimoto, K., Yasui, M., Mori, N., Inoue, T., Shimojima, K., Naito, K., 1984. Galloping phenomena of large bundle conductors experimental results of the field test lines. CIGRE, 22-04.

Nakamura, Y., 1980. Galloping of bundled power line conductors. J. Sound Vib. 73(3), 363–377. https://doi.org/10.1016/0022-460X(80)90521-0.

Nikitas, N., Macdonald, J.H.G., 2014. Misconceptions and generalizations of the Den Hartog galloping criterion. J. Eng. Mech. 140, 04013005. https://doi.org/10.1061/(ASCE)EM.1943-7889.0000697.

Novak, M., 1969. Aeroelastic galloping of prismatic bodies. J. Eng. Mech., 95, pp. 115-142.

Novak, M., 1972. Galloping oscillations of prismatic structures. J. Eng. Mech., 98, pp. 27-46.

Parkinson, G.V., Smith, J.D., 1964. The square prism as an aeroelastic non-linear oscillator. Q. J. Mech. Appl. Math. 17(2), 225–239. https://doi.org/10.1093/qjmam/17.2.225.

Shimizu, M., Shugo, M., Sato, J., 1998. A geometric nonlinear analysis of transmission lines' galloping. J. Struct. Eng. Jpn. 44A, 951–960.

Wang, J., Lilien, J.L., 1998. Overhead electrical transmission line galloping – a full multi-span 3-DOF model, some application and design recommendations. IEEE Trans. Power Deliv. 13(3), 909–915. https://doi.org/10.1109/61.686992.

Yu, P., Desai, Y.M., Shah, A.H., Popplewell, N., 1993. Three-degree-of-freedom model for galloping, Part 1: Formulation. J. Eng. Mech. 119(12), 2404–2425. https://doi.org/10.1061/(ASCE)0733-9399(1993)119:12(2404).

Yukino, T., Fujii, K., Hayase, I., 1995. Galloping phenomena of large bundle conductors observed on the full-scale test line, Proc. Int. Symp. Cable Dyn., Liege, Belgium, 557–563.

Figure Captions

Fig. 1 Cross-sections of ice-accreted four-bundled conductor.

Fig. 2 Aerodynamic coefficients of ice-accreted four-bundled conductor (Matsumiya et al., 2011)

(a) Drag coefficients of sub-conductors

(b) Lift coefficients of sub-conductors

(c) Moment coefficients of sub-conductors

(d) Aerodynamic coefficients of four-bundled conductor

Fig. 3 Den Hartog summation of ice-accreted four-bundled conductor

Fig. 4 Relationship between torsional angle and vertical amplitude with range of relative angle of attack (results of time–history analysis for the vertical 1-DoF system with initial displacement Δy_0 = 5 m)

Fig. 5 Time series of each parameter (vertical 1-DoF system)

(a) $\theta_0 = 38°$

(b) $\theta_0 = 58°$

Fig. 6 Dependency of initial displacement on the vertical amplitude for the vertical 1-DoF system (results of time–history analysis with initial displacement Δy_0 = 0, 1, 2, 3, 4, 5 m)

Fig. 7 Comparison of stable and unstable limit-cycle amplitudes between time–history analysis and energy-balance analysis for the vertical 1-DoF system

Fig. 8 Relationship between non-dimensional amplitude, A_y^*/U^*, and non-dimensional aerodynamic work, E_a^*, for the vertical 1-DoF system

Fig. 9 Dependency of vertical amplitude on torsional frequency ratio for the 3-DoF system

(a) $f_{\theta 0}/f_{y0} = 1.0$

(b) $f_{\theta 0}/f_{y0} = 1.1$

(c) $f_{\theta 0}/f_{y0} = 0.9$

(d) $f_{\theta 0}/f_{y0} = 1.2$

(e) $f_{\theta 0}/f_{y0} = 0.8$

(f) $f_{\theta 0}/f_{y0} = 1.3$

(g) $f_{\theta 0}/f_{y0} = 0.7$

Fig. 10 Comparison of vertical amplitudes between different torsional frequency ratios for the 3-DoF system

(a) All stable solutions larger than zero

(b) Stable solutions in the case with $\Delta_{y0} = 0.0$ m

Fig. 11 Comparison of vertical amplitudes between different horizontal frequency ratios for the 3-DoF system

(a) All stable solutions larger than zero

(b) Stable solutions in the case with $\Delta_{y0} = 0.0$ m

Fig. 12 Comparison of vertical amplitudes between different horizontal and torsional frequency ratios for the 3-DoF system

(a) All stable solutions larger than zero

(b) Stable solutions in the case with $\Delta_{y0} = 0.0$ m

Fig. 13 Oscillation characteristics of 3-DoF galloping (f_{z0}/f_{y0} = 1.0, $f_{\theta 0}/f_{y0}$ = 0.9)

(a) Vertical amplitude

(b) Horizontal amplitude

(c) Torsional amplitude
(d) Amplitude of relative angle of attack
(e) Frequency of oscillation
(f) Horizontal phase difference
(g) Torsional phase difference
(h) Phase difference of relative angle of attack

Fig. 14 Comparison of vertical amplitudes under various DoF systems and frequency ratios (Time–history analysis, Δ_{y0} = 0–5 m)
(a) All stable solutions larger than zero ($\Delta_{y0} = 0$– 5 m)
(b) Stable solutions in the case with $\Delta_{y0} = 0.0$ m

Fig. 15 Time series of each variable compared to those without horizontal velocity at torsional angle $\theta_0 = \theta_s = 56°$ (vertical–horizontal 2-DoF system, $f_{z0}/f_{y0} = 1.0$)
(a) Time series of vertical and horizontal displacements
(b) Time series of vertical and horizontal velocities
(c) Time series of relative wind speed U_r
(d) Time series of relative angle of attack α_r
(e) Time series of α_r, $\dot{y}$, $\widetilde{F_y}$ and $\widetilde{F_y}(\dot{z} = 0)$

Fig. 16 Time series of each variable compared to those without torsional displacement at setup torsional angle $\theta_0 = 65°$ (vertical–torsional 2-DoF system, $f_{\theta 0}/f_{y0} = 0.9$, stationary torsional angle $\theta_s = 67.3°$)
(a) Time series of vertical and torsional displacements
(b) Time series of vertical and torsional velocities
(c) Time series of relative wind speed
(d) Time series of relative angle of attack

Fig. 17 Relationship between non-dimensional amplitude, A_y^*/U^* ($= A_y\omega_{y0}/U$), and non-dimensional aerodynamic work, E_a^*, for the vertical system
(a)Vertical-horizontal 2-DoF system ($A_z/A_y = 0.4, \Phi_z = 180°, A_\theta = 0°$)
(b)Vertical-torsional 2-DoF system ($A_\theta = 15°, \Phi_\theta = 60°, A_z/A_y = 0$)

Fig. 18 Effect of horizontal oscillation for the vertical–horizontal 2-DoF system (largest stable solutions of non-dimensional vertical amplitudes for each torsional angle, upper side of $E_{ac}^* \geq 0$)
(a) Effect of horizontal phase difference Φ_z ($A_z/A_y = 0.4$)
(b) Effect of amplitude ratio between horizontal and vertical oscillations A_z/A_y ($\Phi_z = 180°$)

Fig. 19 Effect of torsional oscillation for the vertical–torsional 2-DoF system (largest stable solutions of non-dimensional vertical amplitudes for each mean torsional angle, upper side of $E_{ac}^* \geq 0$)
(a) Effect of torsional phase difference Φ_θ ($A_\theta = 15°$)
(b) Effect of torsional amplitude A_θ ($\Phi_\theta = 90°$)